

LIBRARY Michigan State University

This is to certify that the thesis entitled

Assessing Turbulence Models for Simulating Gas-Turbine **Endwall Aerodynamics and Heat Transfer**

presented by

Robert D. Draper

has been accepted towards fulfillment of the requirements for the

Master of Science

degree in

Mechanical Engineering

Major Professor's Signature

Date

PLACE IN RETURN BOX to remove this checkout from your record.

TO AVOID FINES return on or before date due.

MAY BE RECALLED with earlier due date if requested.

DATE DUE	DATE DUE	DATE DUE

6/07 p:/CIRC/DateDue.indd-p.1

ASSESSING TURBULENCE MODELS FOR SIMULATING GAS-TURBINE ENDWALL AERODYNAMICS AND HEAT TRANSFER

Ву

Robert D. Draper

A THESIS

Submitted to
Michigan State University
in partial fulfillment of the requirements
for the degree of

MASTER OF SCIENCE

Department of Mechanical Engineering

2007

ABSTRACT

ASSESSING TURBULENCE MODELS FOR SIMULATING GAS-TURBINE ENDWALL AERODYNAMICS AND HEAT TRANSFER

By

Robert D. Draper

The fluid mechanics in gas-turbine endwalls is quite complicated with horseshoe, passage, and corner vortices. These secondary flows adversely affect performance and reliability of gas turbines. This is because secondary flows get their energy from the main flow, and so is a source of aerodynamic loss. Also, they entrain higher-temperature gas in the main flow to the airfoils and the endwalls, and this can increase surface heat transfer. On film cooling, secondary flows can advect and lift film-cooling jets away from surfaces that they are intended to protect. These detrimental effects can be especially severe for low-aspect ratio, high-pressure turbines and highly loaded, low-pressure turbines.

The objective of this research is to assess the usefulness of existing turbulence models in predicting the complicated flow and heat transfer in the endwall region of the first-stage stator. The following models will be evaluated: (1) the realizable k-ε model, (2) the shear stress transport k-ω model with the two-layer model in the near-wall region, (3) Durbin's v2-f model, (4) the Reynolds-stress model with the two-layer model in the near-wall region, and (5) the Spalart-Allmaras model. The evaluation will be performed in two steps. First, a grid sensitivity study will be performed. Afterwards, predictions will be compared with experimental measurements

ACKNOWLEDGEMENTS

The author would like to thank Dr. Tom I-P. Shih for his support in completing the requirements for this Master of Science degree. He has been very supportive and instrumental in learning the necessities of computational fluid dynamics.

The author would like to also thank R. W. Radomsky and K. A. Thole for the use of their experimental data, which serves for comparison to the numerical results generated during this thesis. They have recorded their measurements meticulously and this has made for a comprehensive comparison.

TABLE OF CONTENTS

LIST OF TABLES	v
LIST OF FIGURES	vi
KEY TO SYMBOLS	viii
CHAPTER 1 INTRODUCTION	1 3 16
CHAPTER 2 DESCRIPTION OF PROBLEM	19
CHAPTER 3 DESCRIPTION OF NUMERICAL METHOD OF SOLUTION	23
CHAPTER 4 RESULTS	32
REFERENCES	54

LIST OF TABLES

Table 1: Vane local wall coordinates	26
Table 2: Endwall local wall coordinates	33
Table 3: Case number and file name of each simulation	35
Table 4: Computational information for Cases 1-8	55

LIST OF FIGURES

Figure 1: Wall treatment approaches, wall function is shown at left and near-wall modeling is shown at right.	10
Figure 2: Divisions of near-wall region in fully turbulent flow	12
Figure 3: Schematic of experimental domain used by Radomsky and Thole	14
Figure 4: Numerical domain and boundary conditions for 3D simulations	14
Figure 5: Test section used by Radomsky and Thole.	24
Figure 6: Boundary condition specifications on 3D numerical domain.	26
Figure 7: Vane geometry, shown in meters.	27
Figure 8: Vane locations of experimental measurements	27
Figure 9: Two-dimensional mesh, swept in spanwise direction to create three-dimensional numerical domain.	29
Figure 10: Leading edge region of two-dimensional mesh, swept in spanwise direction create three-dimensional numerical domain.	
Figure 11: Trailing edge region of two-dimensional mesh, swept in spanwise directio create three-dimensional numerical domain.	
Figure 12: Mesh comparison of two-dimensional grid sensitivity cases	33
Figure 13: Numerical domain for all three-dimensional simulations.	34
Figure 14: Residual plot for Case 1.	38
Figure 15: Residual plot for Case 2.	39
Figure 16: Residual plot for Case 3.	40
Figure 17: Plot of wall shear versus vane location for Cases 1, 2, and 3	42
Figure 18: Plot of turbulent kinetic energy versus vane location for Cases 1, 2, and 3,	43

Figure 19: Contour plots of Mach number for Case 1 (top), Case 2 (middle), and Case 3 (bottom)
Figure 20: Contour plots of static pressure (gage) for Case 1 (top), Case 2 (middle), and Case 3 (bottom)
Figure 21: Residual plot for Case 4
Figure 22: Residual plot for Case 5
Figure 23: Residual plot for Case 6
Figure 24: Residual plot for Case 7
Figure 25: Residual plot for Case 8
Figure 26: Endwall heat transfer results in local y-coordinates for y+ = 1 in the numerical domain
Figure 27: Endwall heat transfer results in local y-coordinates for y+ = 5 in the numerical domain
Figure 28: Endwall heat transfer results in local y-coordinates for y+ = 10 in the numerical domain
Figure 29: Endwall heat transfer results in local y-coordinates for y+ = 20 in the

KEY TO SYMBOLS

h	= convective heat transfer coefficient	
k	= turbulent kinetic energy	
Lt	= turbulent lengthscale	
Ma	= Mach number	
P	= stator vane pitch	
P_{gb}	= gage back pressure (for pressure outlet boundary condition)	
P_s	= static pressure	
P_{ι}	= total pressure	
q"	= heat flux	
Re	= Reynolds number	
s	= surface distance along stator vane, measured from flow stagnation	
S	= span of stator vane	
T_{ι}	= total temperature	
$T_{\iota b}$	= total back temperature (for pressure outlet boundary condition)	
Tu	= turbulence level	

C = chord of stator vane

 T_{w} = wall temperature

U =incident upstream velocity

 u_r = shear velocity

X,Y,Z = global coordinates defined from stagnation location

y = normal distance from the wall in Cartesian coordinates

 y^+ = normal distance from the wall in non-dimension, inner wall coordinates

 δ = boundary layer thickness

 ε = turbulent dissipation rate

 θ = displacement thickness

 κ = von Karman constant

 μ = dynamic viscosity

 ν = kinematic viscosity

 v_T = turbulent kinematic viscosity

 ρ = density

 τ_w = wall shear stress

 ω = turbulence frequency

MOTIVATION

The aspiration of this research is to gain a firm understanding of computational fluid dynamics (CFD) and to acquire a working knowledge of the functions necessary to proficiently use a commercial CFD package with confidence. CFD is a design tool that has proven itself in many industries. One such field of interest is that of industrial gas turbines. This area of research incorporates experimental mechanics and theoretical computations. In conjunction with the well known equations of conservation, the primary sources of closure to the systems of equations that model the highly turbulent flows typical to this discipline are based on the results of experimental measurements.

The motivation for this study is to validate the commercially available CFD models in moderate turbulence levels through a stator vane passage. By using the experimental data published by Radomsky and Thole [1], [2], [3], [4] on a PRATT & WHITNEY stator vane, a complete set of initial conditions, boundary conditions, and flow characteristics have been compiled. This data will be used to completely analyze the capabilities of the commercial source code FLUENT 5/6 [5]. FLUENT's preprocessing software, GAMBIT, will be used for all gird generation.

The mesh size for the three dimensional, near-wall model has 1.5 million cells.

All elements generated in this research have been structured, multi-block, quadrilaterals.

Of the turbulent models accessible in FLUENT 5/6, the following have been employed

for this research: realizable k- ϵ , shear stress transport k- ω , Durbin's v^2 -f, Spalart-Allmaras, and the Reynolds stress model. Along with the results provided by Radomsky and Thole, these models were used to benchmark the turbulent flow capabilities of FLUENT 5/6. Error estimation, time per iteration, and computational time required to reach a converged solution are additional aspects of the benchmark study that have been documented for posterity purposes.

LITERATURE SURVEY

While considerable effort has been spent analyzing rotor blades, less emphasis has been placed on stator vane studies. Given the aggressiveness of rotor blade turning angles and flow acceleration versus that customary to stator vanes, the somewhat less complicated physics associated with stator vane passages may be more equipped to learn the correlations between the flowfield and surface heat transfer effects that are typical to turbomachinery [6]. The majority of this research is focused on the effects of heat transfer in the endwall region of the flow passage. The experimental data supplied by Radomsky and Thole provides a baseline for comparison of the results generated with the turbulent models used in FLUENT 5/6. There is a complete set of boundary and operating conditions to properly represent the characteristics of the flowfield. The vane geometry has been supplied by Pratt & Whitney. For the purpose of this research, this blade has been scaled up by a factor of nine.

In CFD, often the most time-consuming task is generating a quality computational domain. Practical turnaround times for computing a solution and availability of computer resources often limit the number of points that can be utilized in a grid. However, when minimizing the number of cells in a given mesh, one must not sacrifice accuracy. As such, grid points must be placed in regions where they are needed most to resolve the geometry and flow physics, but sparsely distributed everywhere else. Unfortunately, this non-uniform distribution can create what are referred to as poor quality cells. Poor quality cells can induce considerable errors in the computed solutions [7]. Qin and Shih advocate

three major sources of error in CFD; inadequate modeling of unresolved physics such as turbulence, spurious modes from discretization of partial differential equations, and errors induced by poor quality or insufficiently fine meshes [8]].

In accordance with the first and second points discussed above, five different models have been employed over the same numerical domain. The default coefficients, as recommended by FLUENT 5/6 documentation [5], have been used appropriately in an effort to minimize unnecessary differences between numerical methods of solution. Mesh quality is the only factor mentioned by Qin and Shih that can be controlled in this research. Such as the case, a grid sensitivity study has been performed in an effort to generate a two-dimensional, grid independent solution. Once optimal cell placement was thought to be attained throughout the vane passage, the final steps in the study were to increase and decrease the grid density by a factor of two or more. The results from this these three cases have been compared as a final indication that the two-dimensional, grid independent solution has been found. The mesh has been swept in the spanwise direction and provides the basis for the three-dimensional domain that has been used for the benchmark study. The grid generation package offered by FLUENT 5/6 is GAMBIT, which has been used for all preprocessing during this research.

GAMBIT is a robust, user friendly program that is well suited for simple geometric domains. It offers translation for the import and export of surface and volume meshes across many platforms, such as ANSYS, PATRAN, I-DEAS, and HyperMesh to

name a few [5]. GAMBIT utilizes a very systematic procedure for generating meshes.

The only criticism made towards the software is in a lack of mesh automation available.

As shown in Figure 1 [5], FLUENT 5/6 offers two techniques for modeling boundary layer fluid flow: wall function and near-wall modeling. Wall functions are typically referred to as high-Reynolds number models and approximate the boundary layer with a log-law relationship, which does not further subdivide the boundary layer.

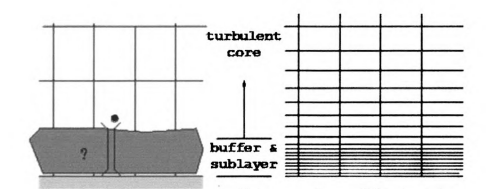


Figure 1: Wall treatment approaches, wall function is shown at left and near-wall modeling is shown at right.

Figure 1 also shows how the wall function approach can significantly reduce the amount of elements in the model and, thus, the computation time spent in the processing phase of the simulation. By approximating the buffer and sublayers of the boundary layer with a log-law relationship, there is no requirement to place grid points inside an inner wall distance of $y^+ = 40$. The variable y^+ is a non-dimensional, inner wall coordinate and is defined in Equation 1.

Equation 1:
$$y^+ = \frac{y \cdot u_\tau}{v}$$

Here, ν is the kinematic viscosity of the fluid, u_r is the shear velocity, which is defined in Equation 2.

Equation 2:
$$u_{\tau} = \sqrt{\frac{\tau_{w}}{\rho}}$$

In Equation 2, τ_w is the wall shear stress and ρ is the density of the fluid. In the most simplistic case, for flow over a flat plate with no pressure gradient, the form of the shear stress is defined by Equation 3. As shown below, U is the velocity component of the core flow parallel to the flat plate and x is in the direction of the flow.

Equation 3:
$$\tau_w = \rho \cdot U^2 \cdot \frac{d\theta}{dx}$$

By definition, θ is the momentum thickness of the boundary layer and is defined in Equation 4. The momentum thickness is based on the fact that the boundary layer thickness, δ , is some distance normal to the wall such that at $\delta = y$, $u = .99 \cdot U$. In Figure 2 [5], the velocity profiles that make up the boundary layer for two turbulent flows are shown.

Equation 4:
$$\theta = \int_{0}^{\infty} \frac{u}{U} \left(1 - \frac{u}{U} \right) dy$$

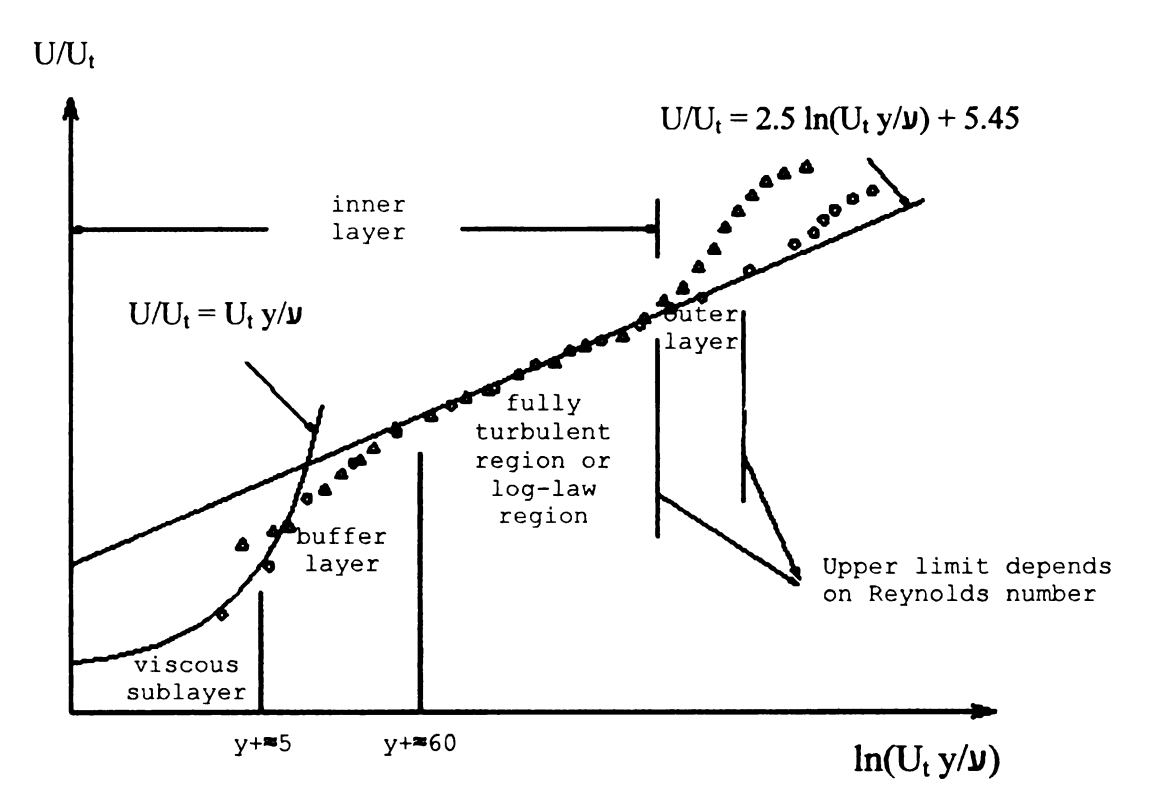


Figure 2: Divisions of near-wall region in fully turbulent flow.

As described by van Driest [9], "...fully developed turbulent motion occurs only beyond a distance sufficiently remote from the wall that the very eddies themselves are not damped in turn by the nearness of the wall." As such, the wall function approach is adequate if only a broad understanding of the physics at work in the flow domain is desired. As shown in Figure 2, the log-law relationship very closely follows the velocity profiles outside of the viscous sublayer and buffer layer, where viscosity affect are negligible on the core flow. Therefore, if boundary layer interactions are of interest, the grid should meet this requirement and extend all of the way to the wall.

For situations where low-Reynolds-number effects are dominant and of interest, near-wall modeling is used to resolve the boundary layer of the flow completely. In this

approach, the mesh extends all of the way to the wall. This method can be extremely comprehensive and, in order to accurately represent the boundary layer, usually requires significantly large grids.

In the wall function approach, the numerical domain is further discretized to reduce grid resolution at the expense of solution accuracy. Since the focus of this research is on endwall heat transfer through the vane passage, all grids have been generated using the near-wall approach to promote accuracy of the computed shear stress and heat transfer coefficients. When measured in local wall coordinates; in the direction normal to the wall, the first grid point is within $y^+ = 1$ and the first ten grid points are located within $y^+ = 10$.

Another function of the mesh is for the application of boundary and operating conditions. Inlet, exit, symmetry conditions, as well as wall boundaries and other physical conditions are numerically incorporated onto the domain. Figure 3 illustrates the experimental domain used by Radomsky and Thole [1]. Figure 4 depicts the numerical domain and the locations where boundary conditions (BCs) have been applied. As shown below, a single vane passage has been used to represent the test section. So that proper mesh quality and adequate grid resolution could be accomplished in modeling one vane passage, symmetry boundary conditions have been specified as the pitchwise boundaries.

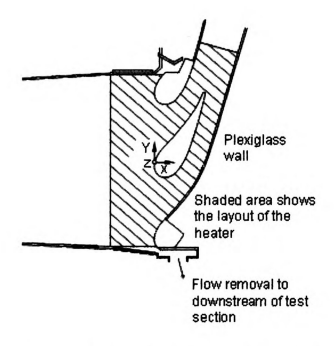


Figure 3: Schematic of experimental domain used by Radomsky and Thole.

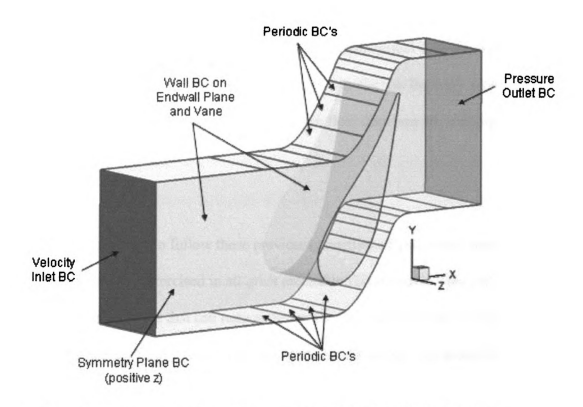


Figure 4: Numerical domain and boundary conditions for 3D simulations.

Mesh quality is attributed by node distribution, smoothness, and skewness. Along with proper clustering at the leading edge of the vane, smooth transitioning between cells in the flow direction and minimizing skewness are critical aspects of quality grids.

Smoothness is a measure of change between adjacent cell volumes. Rapid changes lead to truncation errors, which are the differences between the partial derivatives of the governing equations and their discrete approximations [5]. Skewness is a measure of the difference in shape between cells of similar volume and optimal quadrilateral cells have near-orthogonal vertex angles. These mesh attributes are used to keep numerical diffusion to a minimum, while encouraging accuracy and stability.

Numerical diffusion is a dominant source of error in multidimensional domains. It is most noticeable in convection-dominant problems, where physical diffusion is small.

All numerical schemes contain a finite amount of numerical diffuser, which arises from truncation errors in representing flow equations in discrete form [5]. However, proper mesh refinement and alignment of cells to the flow direction are techniques that minimize numerical diffusion.

In an effort to follow these previously mentioned guidelines, quadrilateral cell shapes have been exercised in all grids created in this research. This cell shape is capable of large aspect ratios that can reduce the number of cells necessary to sufficiently resolve the flow domain in the streamwise and spanwise directions. Numerical diffusion, stability, and accuracy can be further controlled by solution strategies.

The FLUENT 5/6 software package offers a wide variety of solver options and solution strategies. The characteristics of the numerical method of this software are double precision, segregated, implicit scheme that is incorporated over a pressure-based flow solver. Second-order upwind discretization has been utilized for convection terms, while second-order central differencing has been used for diffusion terms, and pressure and velocity coupling has been achieved through the use of the Semi-Implicit Method for Pressure-Linked Equations (SIMPLE) algorithm.

The Spalart-Allmaras model uses one transport equation to solve for the turbulent viscosity, ν_T . It was designed specifically for aerospace applications involving wall-bounded flows and is being used for turbomachinery applications as well. The Spalart-Allmaras model represents a family of one-equation transport models that do not require the calculation of the length scale related to the local shear layer thickness. As a result, criticism has been placed on one-equation models for their inability to rapidly accommodate changes in length scale, which may be noticed as the flow changes from that of a wall bounded flow to free shear flow. The transport equation for the Spalart-Allmaras model is shown in Equation 5, with S_{ν} being the source term.

Equation 5:
$$\frac{\overline{D}v_T}{\overline{D}t} = \nabla \cdot \left(\frac{v_T}{\sigma_v} \nabla v_T\right) + S_v$$

The Spalart-Allmaras model is effectively a low-Reynolds-number model that has been shown to provide good results for boundary layers subjected to adverse pressure gradients of the transported variable being much smaller than those in the realizable k-s

and shear stress transport k-ω models. As described by Pope [10], an accelerating flow produces a negative or favorable pressure gradient, while decelerating flow generates positive or adverse pressure gradients. The adverse pressure gradient is so called because it can lead to separation of the boundary layer from the surface, which is typically not desirable for turbomachinery applications.

The realizable $k-\epsilon$ model is based off of the standard $k-\epsilon$ model with the exceptions of new formulations for the turbulent viscosity and transport equation for the dissipation rate [5]. "The term "realizable" means that the model satisfies certain mathematical constraints on the Reynolds stresses, consistent with the physics of turbulent flows [5]." Thus, the realizable $k-\epsilon$ model performs well in boundary layer flows experiencing separation, recirculation, and strong adverse pressure gradients. Due to the inclusion of mean rotation effects in the definition of the turbulent viscosity, the realizable $k-\epsilon$ model predicts non-physical results of the turbulent quantity when both stationary and rotating fluid zones exist in the computational domain [5]. The realizable $k-\epsilon$ model requires approximately twice the computational effort of the Spalart-Allmaras model. The transport equations for the $k-\epsilon$ model are shown in Equation 6 and Equation 7, where k is the turbulent kinetic energy and ϵ is the turbulent dissipation rate.

Equation 6:
$$\frac{\overline{D}k}{\overline{D}t} = \nabla \cdot \left(\frac{v_T}{\sigma_k} \nabla k\right) + \mathbf{P} - \varepsilon$$

Equation 7:
$$\frac{\overline{D}\varepsilon}{\overline{D}t} = \nabla \cdot \left(\frac{v_T}{\sigma_{\varepsilon}} \nabla \varepsilon\right) + C_{\varepsilon 1} \frac{P\varepsilon}{k} - C_{\varepsilon 2} \frac{\varepsilon^2}{k}$$

In general, the turbulent kinetic energy, turbulent dissipation rate, and turbulent viscosity are related by Equation 8, as described by Pope [10].

Equation 8:
$$v_T = \frac{cC_D k^2}{\varepsilon}$$

The shear stress transport k- ω model is similar to the standard k- ω model. It effectively blends the k- ω model in the low-Reynolds-number region with that of the k- ε model in the core flow. Some of the differences between the shear stress transport k- ω and the standard k- ω model are that the shear stress transport k- ω model incorporates a damped cross-diffusion derivative in the ω transport equation, and the turbulent viscosity accounts for the transport of turbulent shear stress. The shear stress transport k- ω model is similar to the realizable k- ε model in terms of computation time, as they both use two transport equations for closure of turbulence quantities. The turbulence frequency, ω , is the ratio of k/ε and its transport equation is shown in Equation 9.

Equation 9:
$$\frac{\overline{D}\omega}{\overline{D}t} = \nabla \cdot \left(\frac{v_T}{\sigma_\omega} \nabla \omega\right) + C_{\omega 1} \frac{P\omega}{k} - C_{\omega 2} \omega^2$$

The Reynolds stress model uses differential transport equations to calculate the specific Reynolds stresses, which are then used to resolve the Reynolds-averaged momentum equations [5]. The is the most computationally intensive turbulence model offered by FLUENT 5/6, since it closes the Reynolds-averaged Navier Stokes equations by solving transport equations for all of the Reynolds stresses as well as an equation for the dissipation rate. The equation for the evolution of Reynolds stresses is shown in

Equation 10, where the three terms inside the partial derivative are the viscous diffusion, pressure transport, and turbulent convection respectively.

Equation 10:
$$\frac{\overline{\overline{D}}}{\overline{D}t} \langle u_i u_j \rangle + \frac{\partial}{\partial x_k} \left(T_{kij}^{(v)} + T_{kij}^{(p')} + T_{kij}^{(u)} \right) = P_{ij} + \Re_{ij}^{(a)} - \varepsilon_{ij}$$

The v^2 -f model is based on Durbin's k- ε - v^2 model and is similar to the standard k- ε model, but incorporates near-wall turbulence anisotropy and non-local pressure strain effects. Pope [10] defines turbulence isotropy as any flow field that is statistically homogeneous, which under translations is said to be statistically invariant. A statistically isotropic field requires the field to be statistically invariant under rotations and reflections of the coordinate system as well as under translations. Here, the velocity variance (v^2) is the variance of the normal velocity and is used to calculate the eddy viscosity, rather than using the turbulent kinetic energy for determining the eddy viscosity. For this reason, v^2 -f model has been shown to provide improved scaling in representing the damping of the turbulent transport close to the wall [5]. Please reference the user manual for FLUENT 5/6 [5] for a description of the transport equations used in the v^2 -f model.

Convergence criteria is based on the default setting in FLUENT 5/6, which enables scaling of the residuals and requires 10⁻⁶ for energy and P-1 equations, with 10⁻³ for all other equations. Once this level is attained, the results are checked for constancy between solutions from prior iterations. Although this does not substantiate convergence, attaining such a small residual should establish a converged solution. Once the solution

achieves this residual state, the solution is then checked for convergence by calculating the difference of the solution outputs between successive iterations.

When considering computational resources, the two major physical dependences to computation time are processor speed and the amount of random access memory (RAM) the system has access to. As a rule of thumb, a one-million node model will require about one gigabyte of system memory. All computations for this research were computed using FLUENT's parallel solver on a computer with dual, 2.8 MHz processors and 2 gigabytes of random access memory (RAM) operating on Linux RedHat Workstation 3.0. Depending on the turbulent model being solved, the time per iteration over the three-dimensional domain ranged from about 25 seconds for the Spalart-Allmaras model to around 3.25 minutes for the RSM.

OBJECTIVES

There are two objectives for this research. The first is to perform a 2D grid sensitivity study and attain a 2D grid independent solution. The results from this will serve as the basis for the 3D domain. Once this is complete, the experimental results of Radomsky and Thole will be used as a baseline for performing a benchmark study consisting of the following five turbulent models of those available in FLUENT 5/6: realizable k-ε, shear stress transport k-ω, Durbin's v2-f, Spalart-Allmaras, and the Reynolds stress model.

There are numerous turbulent models offered in FLUENT 5/6, which makes for a diverse and interesting benchmark. The goal of the benchmark is twofold. The first intention is to gain an understanding as to which model(s) most accurately depict the experimental data generated by Radomsky and Thole [1], [2], [3], [4].

APPROACH

In order to demonstrate the turbulent modeling capabilities of the commercially available source code in FLUENT 5/6, no other software has been used during the preprocessing and solver phases of this research. GAMBIT has been used to complete all grid generation. By constructing an over developed near-wall region in the mesh, a highly resolved boundary layer will be captured for comparison to the experimental data of Radomsky and Thole [1], [2], [3], [4].

Numerous iterations were made to the 2D domain in an effort to attain the grid independent solution for this stator vane passage and operating and boundary conditions. The 2D grid sensitivity study provides confidence that the mesh adequately represents the physics at work in this flow regime. Although time consuming, this task is necessary for providing vital information on cell placement throughout the computational domain. Upon arriving at a mesh that provided an acceptable solution, the node densities were both increased and decreased by a factor of at least two times that of the original grid density. The solutions to these three different meshes were then compared against each other on the basis of skin friction coefficient, pressure coefficient, and other flow characteristics to verify that the grid independent solution had been reached.

In order to completely capture the physics at work in the boundary layer of the vane passage, all meshes created for this research are based on near-wall modeling

techniques. When measured in local wall coordinates, the first grid point is located at y^+ < 1 and the first ten grid points are located within y^+ = 10. The 2D mesh produced during the sensitivity study has been swept in the spanwise direction to construct the 3D domain necessary for the benchmark study to simulate the experimental geometry used by Radomsky and Thole [1].

Convergence criteria is based on the default setting in FLUENT 5/6, which enables scaling of the residuals and requires 10⁻⁶ for energy and P-1 equations, with 10⁻³ for all other equations. Once this level is attained, the results are checked for constancy between solutions from prior iterations. Although post processing can be accomplished in FLUENT 5/6, Tecplot has been used for all plotting and visualization.

DESCRIPTION OF PROBLEM

The test section used by Radomsky and Thole [1] consists of one centralized vane and two partial vanes, as shown in Figure 5. The Cartesian coordinate system shown below has been utilized for all simulations. The vane has a chord length, C, of .594 meters and a span, S, of .552 meters. The pitch, P, of the vane cascade is .457 meters. As shown below, the vertical or y-axis is aligned with the pitchwise direction and the z-axis corresponds to the spanwise direction, with the x-axis being parallel to the inlet flow direction.

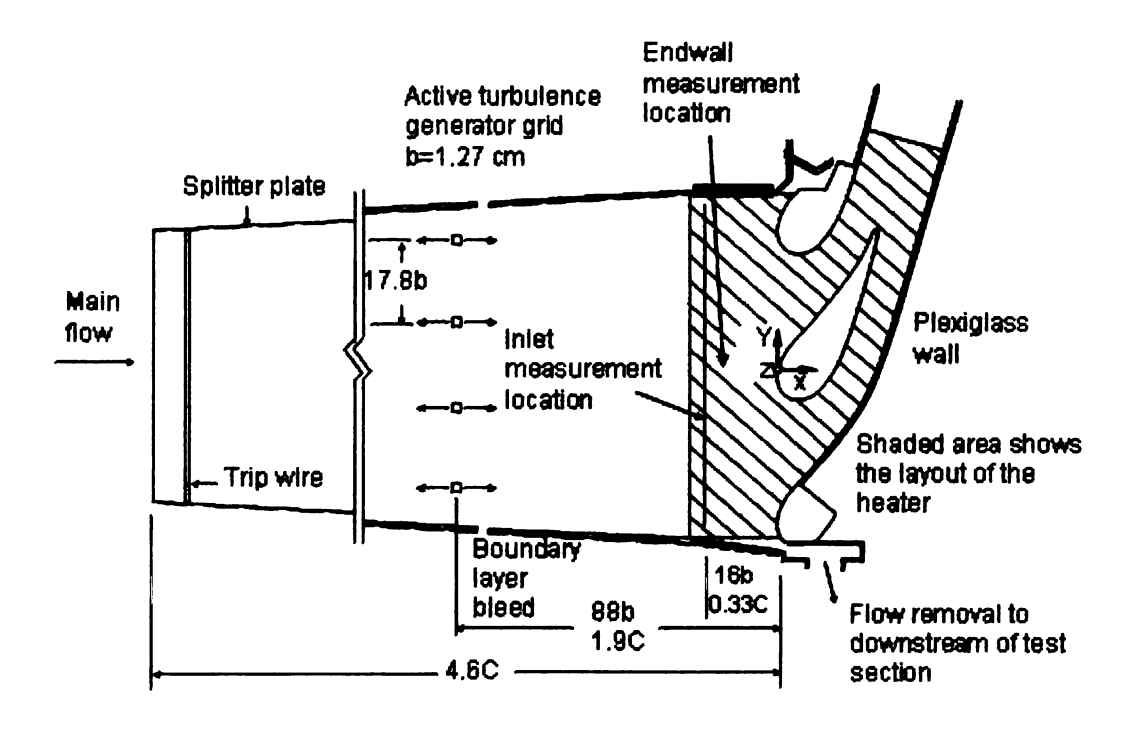


Figure 5: Test section used by Radomsky and Thole.

In order to simulate the test section numerically, a velocity inlet boundary condition was enforced at a distance of one chord length upstream of the vane leading

edge in a location where the velocity field is unaffected by the presence of the vane. This provides uniform flow through the vane passage and matches the inlet Reynolds number of 230,000 used in the experiment. A user-defined function was used to specify the endwall boundary layer profile on the inlet plane. A pressure outlet boundary condition was imposed at a distance of one chord length downstream of the vane's leading edge to reduce numerical errors in the solution by placing the boundary location downstream of the wake mixing region in the flow.

A constant heat flux boundary condition has been applied to the grid in a fashion similar to that used by Radomsky and Thole [3] in the experiment with a heater on the endwall. Since the passage is symmetric in the spanwise direction, the computational grid was made to be only half of the physical geometry. In doing so, the mesh was able to be clustered more closely to the endwall. All of the boundary conditions and their values are shown in Figure 6.

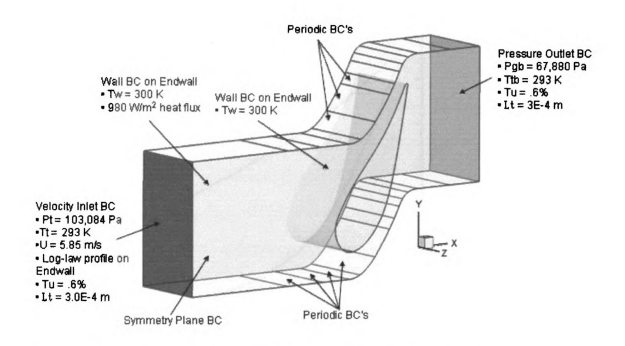


Figure 6: Boundary condition specifications on 3D numerical domain.

The vane profile is shown in Figure 7. The original coordinates are from a PRATT & WHITNEY stator vane, which has been scaled up by a factor of nine for this work. Experimental results have been measured at nine different locations along the vane profile, as presented by Radomsky and Thole [4] and shown below in Figure 8. Here, the variable s/C is the ratio of distance around the vane profile measured from the stagnation location and divided by the chord length.

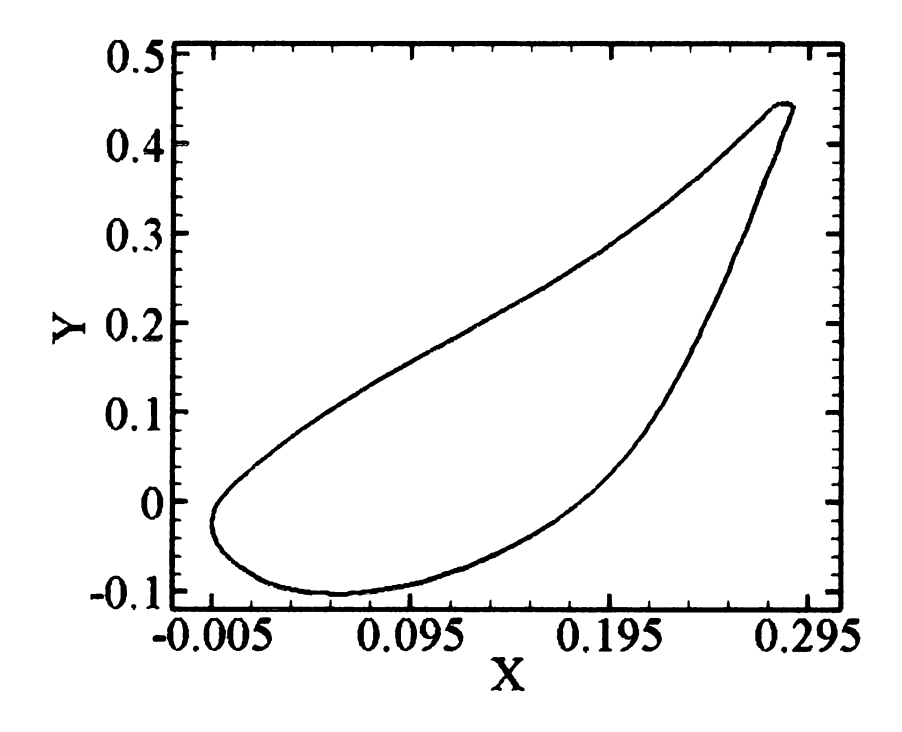


Figure 7: Vane geometry, shown in meters.

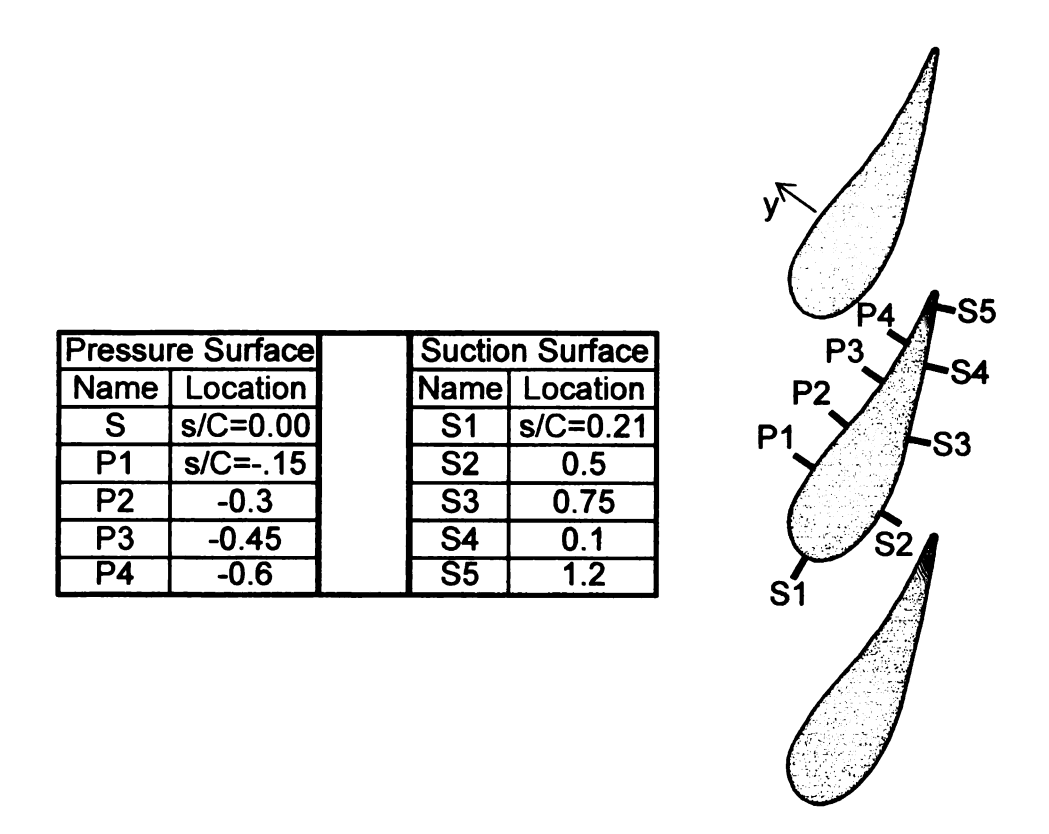


Figure 8: Vane locations of experimental measurements.

DESCRIPTION OF NUMERICAL METHOD OF SOLUTION

The first step to generating a structured, three-dimensional grid is to construct a structured, two-dimensional mesh that can then be swept in the out of plane direction.

This mesh consists of a near wall modeling approach and adheres to the guidelines set forth by Shih [11], with the first 10 grid points being located at the local wall distances indicated in Table 1. In order to fully capture the boundary layer effects through the vane passage, much effort has spent in generating an over developed near-wall region. This is why the first ten grid points are very close to the wall and an aspect ratio near unity has been employed through this region to facilitate constant spacing.

Cell Location	у	y+
Wall	0.000E+00	0.000
1	7.616E-06	0.975
2	8.062E-06	1.032
3	8.062E-06	1.033
4	8.944E-06	1.146
5	8.944E-06	1.147
6	9.849E-06	1.264
7	9.849E-06	1.265
8	1.030E-05	1.323
9	1.118E-05	1.437
10	1.118E-05	1.438
11	1.253E-05	1.613

Table 1: Vane local wall coordinates.

Figure 9 shows the two-dimensional mesh that provides the baseline geometry for the three-dimensional domain. This mesh was produced during the grid sensitivity study and has 50.396 elements.

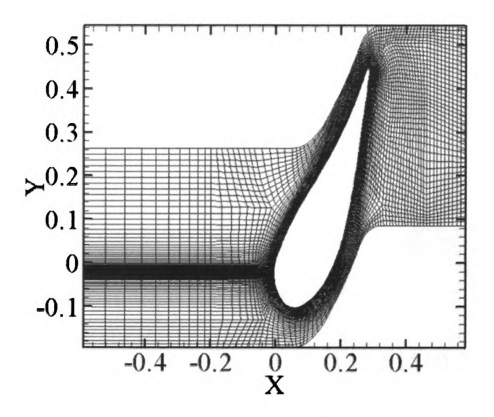


Figure 9: Two-dimensional mesh, swept in spanwise direction to create threedimensional numerical domain.

Much effort was put forth in adhering to the aforementioned grid quality measures. Cell location and aspect ratio have all been optimized by hand in an iterative process that took nearly eighty attempts to achieve the grid shown. This grid has been created using a multi-block approach, as evident in Figure 10 and Figure 11. The multi-block technique allows for relatively smooth transitions in regions where the flow is

expected to turn about the vane profile. Quadrilateral element shape allows for stretching of the cells in the flow direction, while at the same time allowing for near orthogonal intersections between adjacent cells.

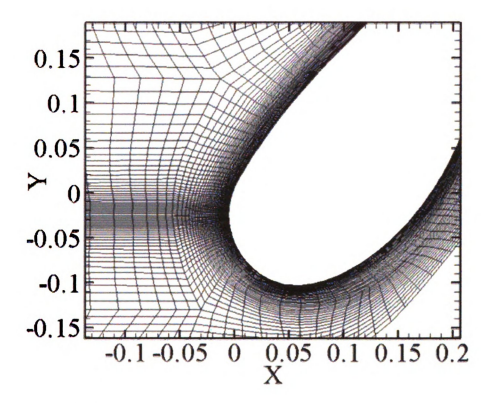


Figure 10: Leading edge region of two-dimensional mesh, swept in spanwise direction to create three-dimensional numerical domain.

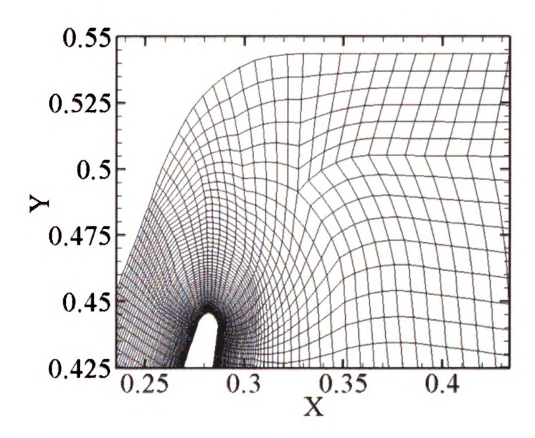


Figure 11: Trailing edge region of two-dimensional mesh, swept in spanwise direction to create three-dimensional numerical domain.

For the purposes of the grid sensitivity study, the two-dimensional mesh shown above has been increased and decreased in node density by at least a factor of two.

Decreasing the mesh density by a factor of two created a grid that consisted of 22,060 elements. This mesh is shown in the top row of Figure 12, with the original mesh shown in the middle row for comparison. While keeping the near-wall region similar to that of the initial mesh, the majority of the cells have been removed by transitioning from the buffer layer to the inner and outer layers by increasing the aspect ratio much more aggressively.

The bottom row of Figure 12 depicts the mesh where the node density has increased by a factor of nearly four times that of the original two-dimensional domain. This mesh consists of 200,544 elements. This mesh transitions from adjacent multi-block regions very smoothly, with good orthogonal qualities, minimal skewness, and is an overall high quality mesh.

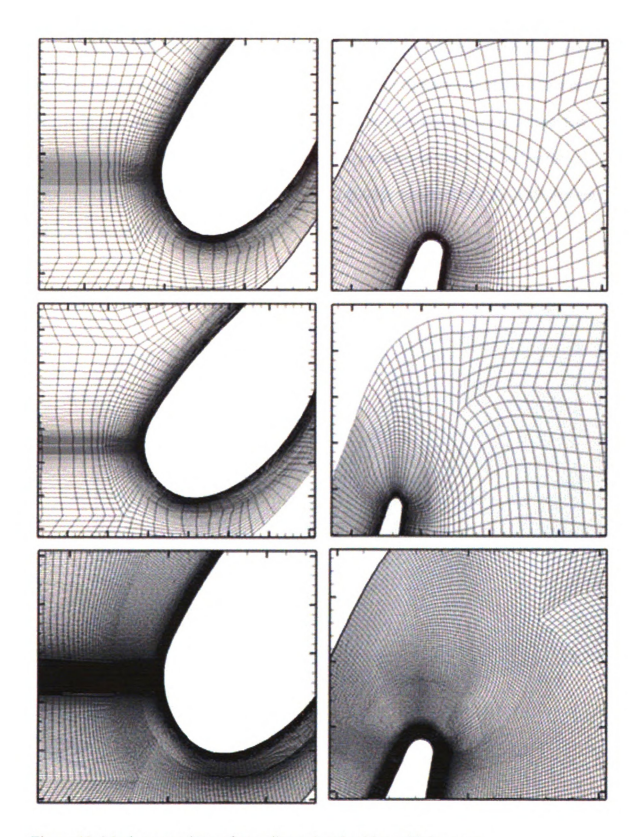


Figure 12: Mesh comparison of two-dimensional grid sensitivity cases.

The two-dimensional mesh shown in Figure 9, Figure 10, and Figure 11 has been swept in the spanwise direction to produce the full, three-dimensional mesh shown in Figure 13. For the three-dimensional simulations, a symmetry boundary condition has been enforced at the midspan location of the vane geometry so that only half of the experimental domain needed be simulated. This grid is comprised of 1,511,880 elements, with 30 cells in the spanwise direction.

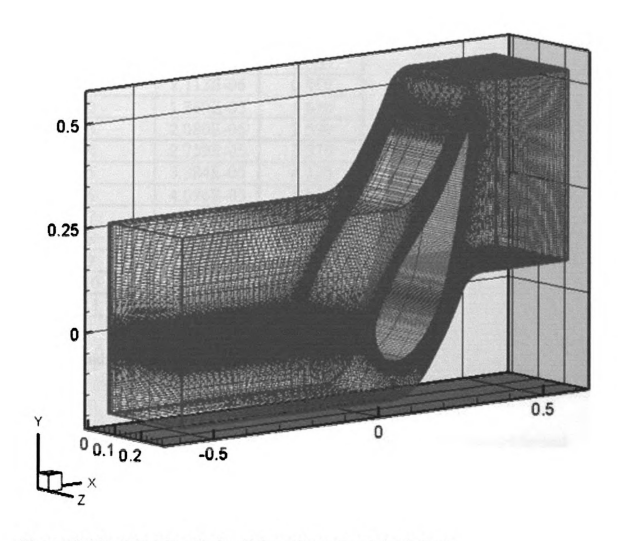


Figure 13: Numerical domain for all three-dimensional simulations.

The three dimensional mesh utilizes the two dimensional grid at the endwall and at each consecutive spanwise node location from the endwall. The first spanwise location in the enhanced wall function grid is at an inner wall distance of y+=0.868 from the endwall. The fifth point is at an inner wall distance of y+=4.135. Table 2 shows the inner wall distance versus node number for the three-dimensional, near-wall modeled grid.

Cell Location	у	y+	
Wall	0.000E+00	0.000	
1	7.113E-06	0.868	
2	1.369E-05	1.670	
3	2.080E-05	2.539	
4	2.759E-05	3.370 4.135 5.006	
5	3.384E-05		
6	4.096E-05		
7	4.861E-05	5.944	
8	5.551E-05	6.791	
9	6.262E-05	7.664	
10	6.909E-05	8.458	
11	7.620E-05	9.334	

Table 2: Endwall local wall coordinates.

All two-dimensional and three-dimensional simulations have been performed using the double precision, segregated solver in FLUEN 5/6. The Semi-Implicit Method for Pressure-Linked Equations (SIMPLE) algorithm has been used in the FLUENT 5/6 pressure-based flow solver for pressure and velocity coupling [5]. Second-order upwind discretization has been used for convection terms and second-order central differencing

has been used for diffusion terms. Under-relaxation parameters have been left at their default settings unless otherwise stated. Convergence criteria are set as the defaults supplied by FLUENT 5/6, with the energy and P-1 equations requiring 10⁻⁶ and all other equations demanding a magnitude of 10⁻³ on the scaled residual.

RESULTS

In total, eight different results will be discussed in the following section. Table 3 shows the file name and turbulent model associated with it. The FLUENT files have been saved at different points along the solution process, so only the name of the converged solution is referenced in Table 3.

Case Number	Mesh File (.msh)	FLUENT Files (.cas, .dat)	Turbulence Model	
1	VTvane92_2D	VTvane92_ralizable_2D_27657	Spalart-Allmaras	
2	VTvane92_Halfx_2D	VTvane92_Halfx_2D_25955	Realizable k-ε	
3	VTvane92_2x_2D	VTvane92_2x_2D_73020	Realizable k-ε	
4	VTvane92_3D	VTvane92_rea_16243	Realizable k-ε	
5	VTvane92_3D	VTvane92_rsm_19892	Reynold's Stress Model	
6	VTvane92_3D	VTvane92_sa_29442	Spalart-Allmaras	
7	VTvane92_3D	VTvane92_3D_sst_26527	Shear Stress Transport k-ω	
8	VTvane92_3D	VTvane92_3D_v2f_15060	Durbin's V2-f	

Table 3: Case number and file name of each simulation.

Cases 1-3 have been performed in support of the two-dimensional, grid sensitivity study. Case 1 refers to the mesh consisting of 50,396 elements referred to in the previous section, with Case 2 being comprised of 22,060 cells, and Case 3 having 200,544 elements. Cases 4-8 constitute the results for benchmarking and comparison to the experimental data of Radomsky and Thole. All of these cases make use of three-dimensional grid containing 1,511,880 elements.

Case 1 was unexpectedly solved with the Spalart-Allmaras turbulent model, so unfortunately a direct comparison can not be made between it and Cases 2 and 3. Figure 14 shows the un-scaled residual versus iteration number for Case 1. Here, convergence is reached for all quantities and this plot shows how each variable reduces by at least three orders of magnitude throughout the iteration process.

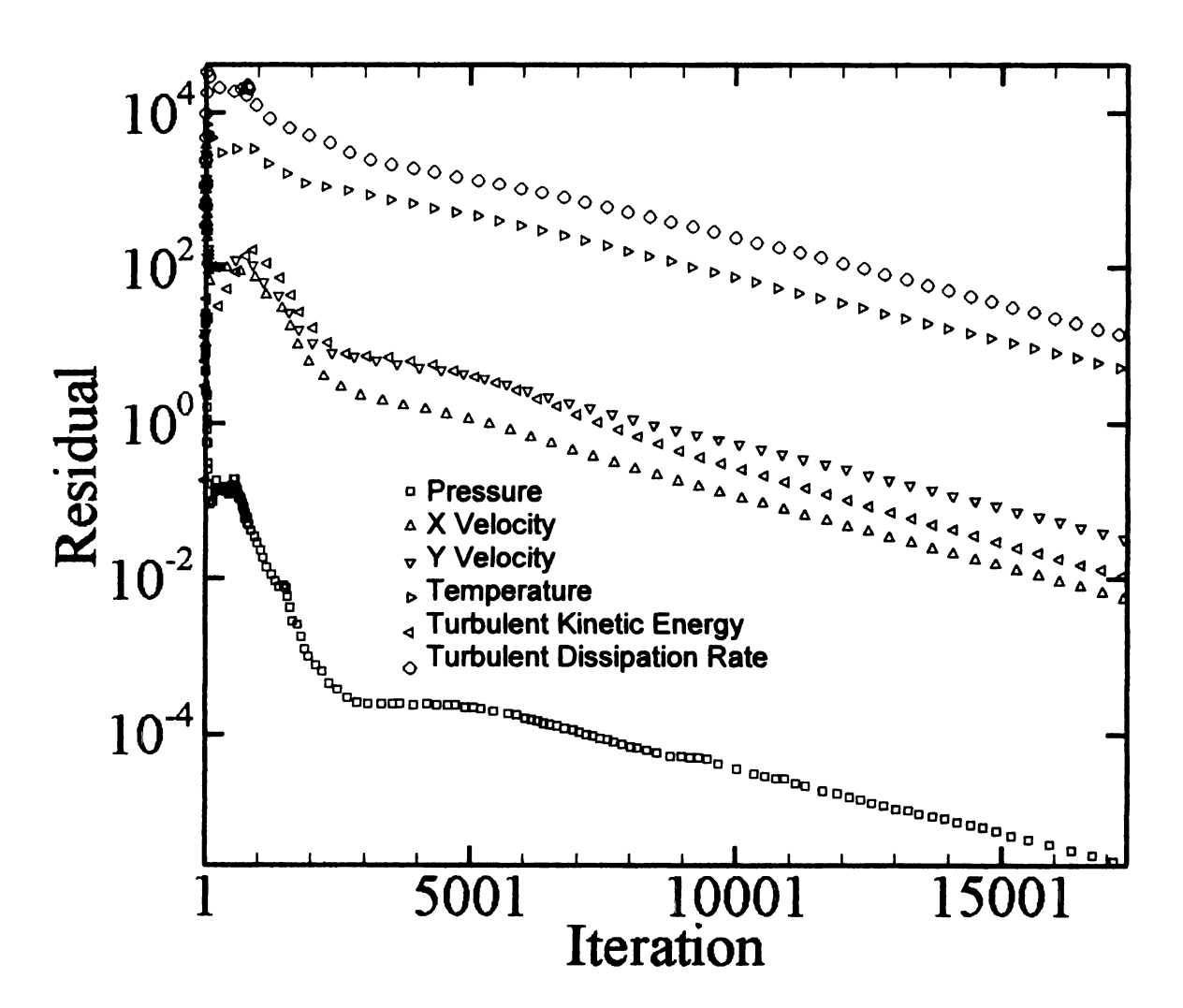


Figure 14: Residual plot for Case 1.

Figure 15 shows the un-scaled residual versus iteration number for Case 2, which was solved with the realizable k- ϵ turbulent model. Again, convergence is reached for all quantities and each variable reduces by at least three orders of magnitude throughout the iteration process.

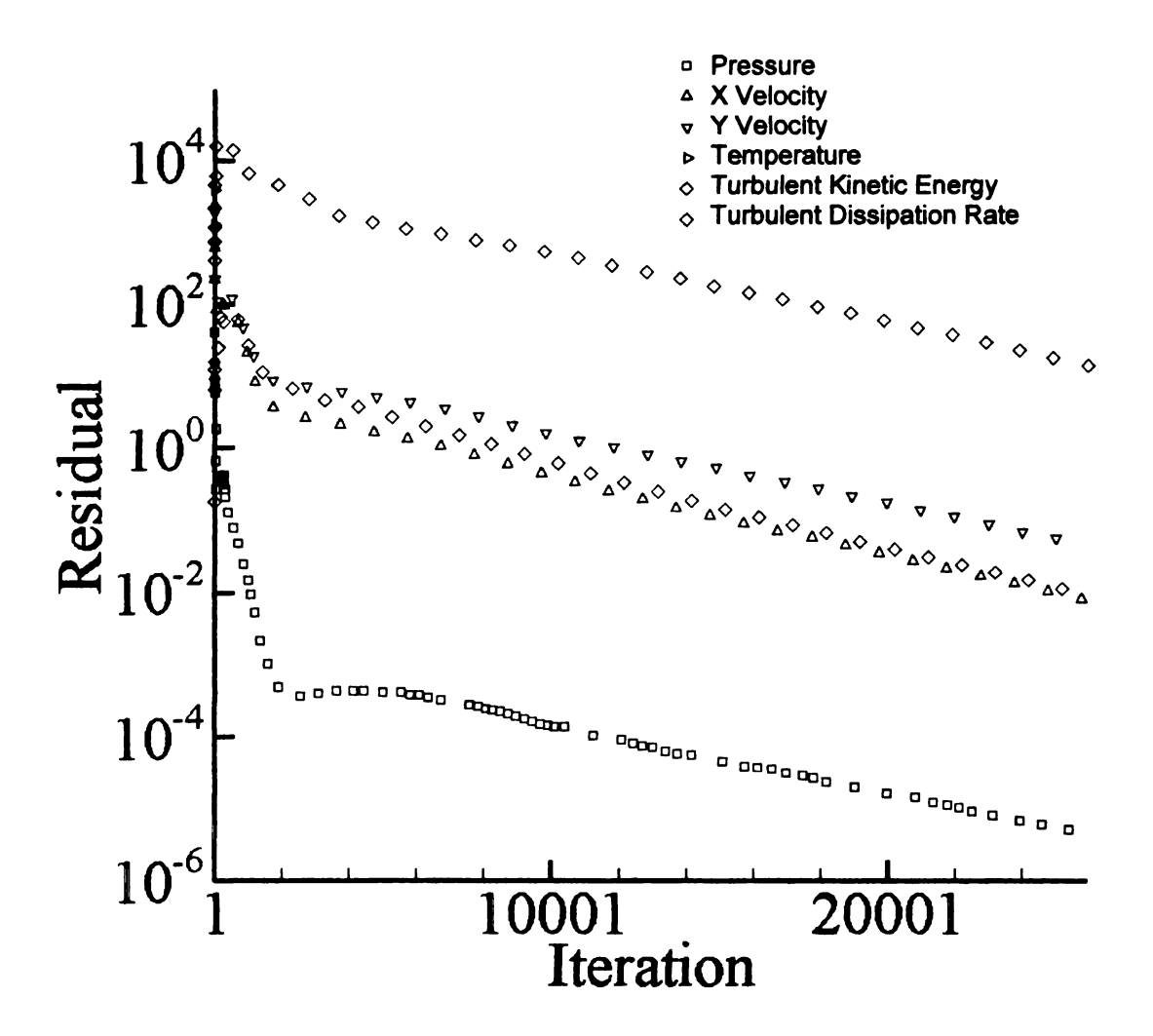


Figure 15: Residual plot for Case 2.

Figure 16 is a plot of the un-scaled residual versus iteration number for Case 3.

This case was solved with the realizable k-ε turbulent model. It can be seen that just after

35,000 iterations the under-relaxation parameters were adjusted to minimize the oscillations seen in the solution. After making this adjustment, the iteration process behaved as expected and it took just under 40,000 iterations to attain a converged solution.

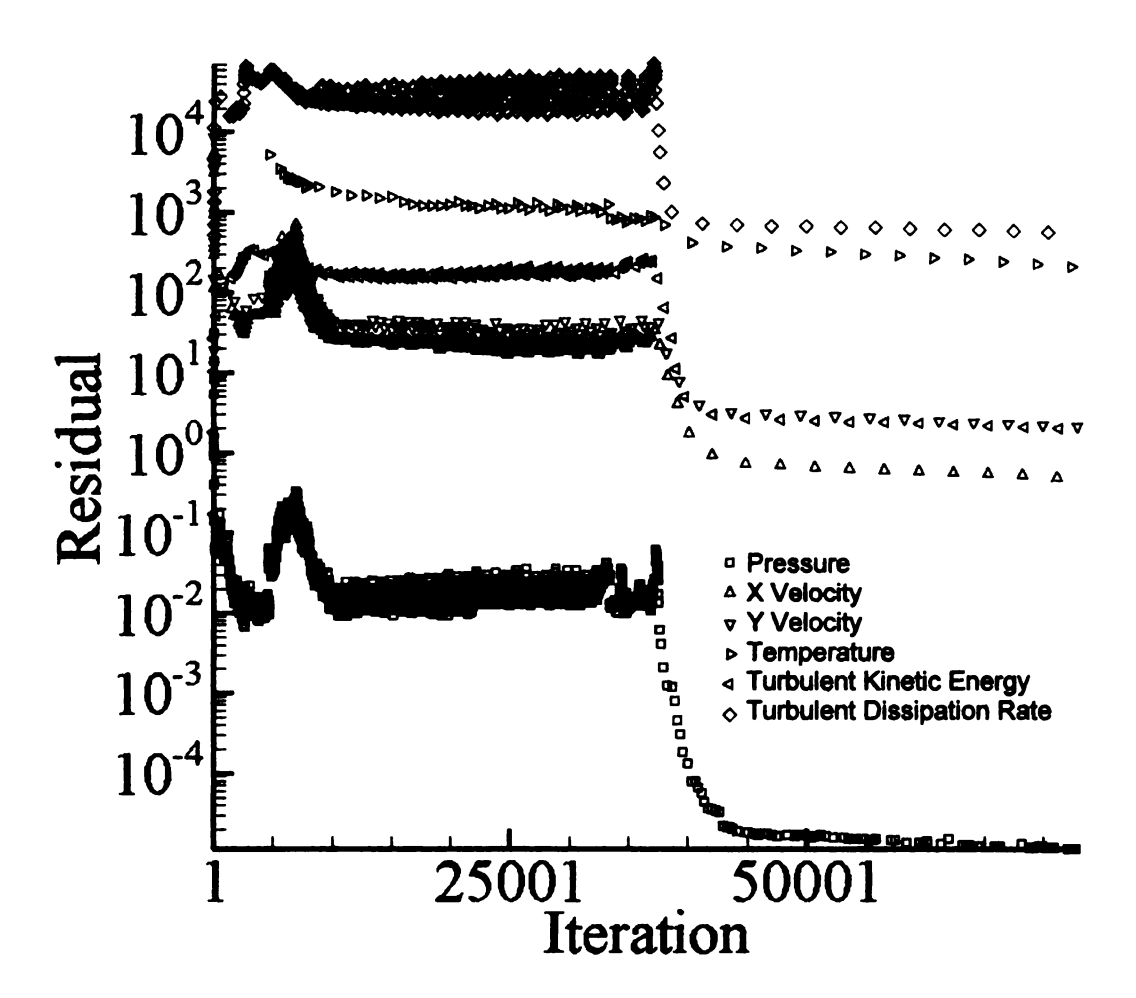


Figure 16: Residual plot for Case 3.

Comparison of Cases 1-3 are shown in the following figures. Here, s/C corresponds to vane locations, with zero indicating the location of stagnation on the vane surface. Decreasing negative values indicate moving along the pressure side of the vane

profile in the direction from the leading edge toward the trailing edge. Increasing positive values represent moving along the suction side of the vane in the direction from the leading edge toward the trailing edge, as shown in Figure 8.

Figure 17 is a plot of wall shear stress (units of Pascal) versus non-dimensional vane location. This plot clearly indicates that all cases are in very good agreement until the flow starts to separate at a vane location of s/C = .7, which is near measurement location S3 in Figure 8. After this point, Case 1 and Case 2 remain in good agreement through the rest of the vane passage. A similar trend is noticed in Figure 18, which is a plot of turbulent kinetic energy versus non-dimensional vane location.

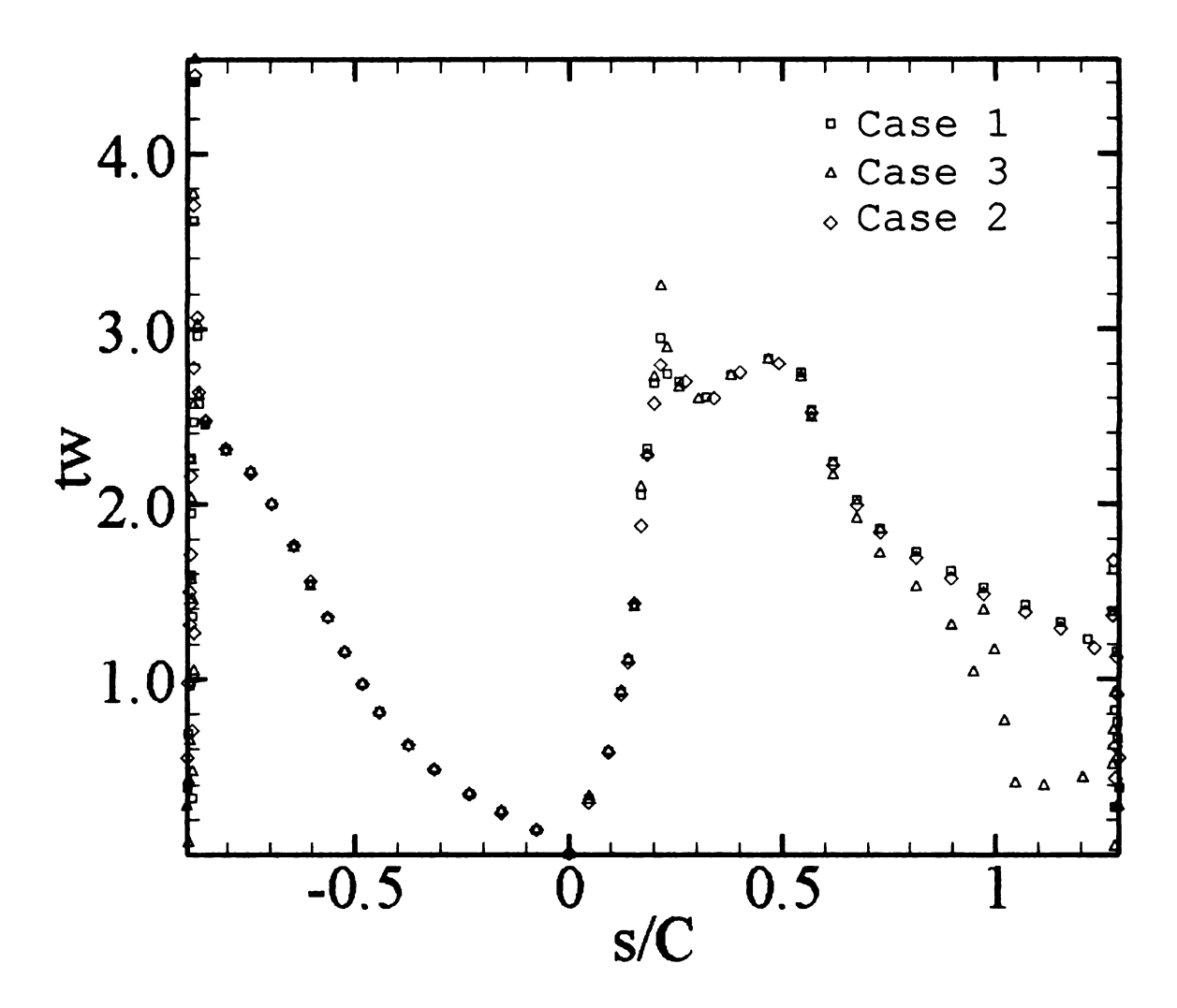


Figure 17: Plot of wall shear versus vane location for Cases 1, 2, and 3.

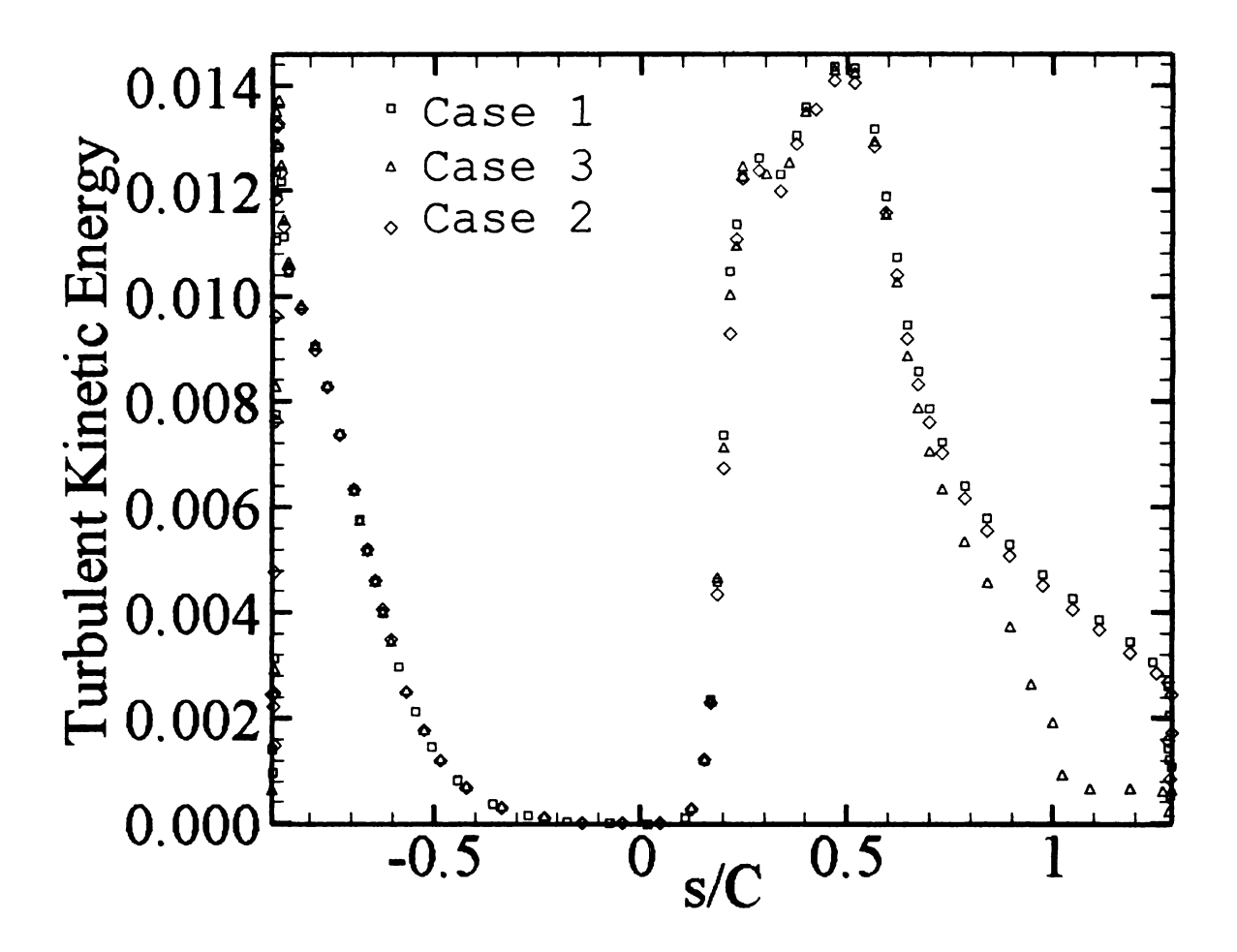


Figure 18: Plot of turbulent kinetic energy versus vane location for Cases 1, 2, and 3.

Contour plots of Mach number and static pressure are shown in the following two figures. Both

Figure 19 and Figure 20 are consistent with the previous two plots in that Case 3 is far superior in predicting the wake region of the flow. This should be expected, since the mesh density is vastly greater than both Case 1 and Case 2.

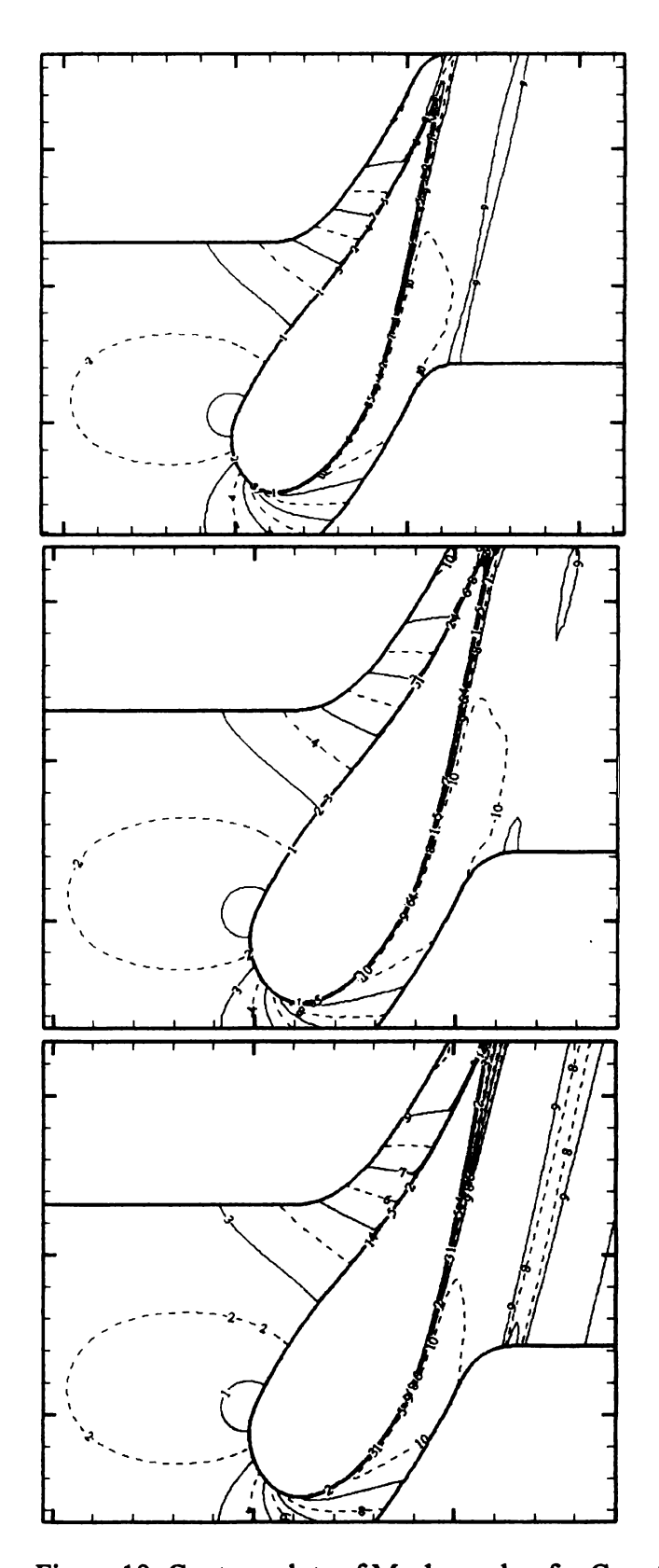


Figure 19: Contour plots of Mach number for Case 1 (top), Case 2 (middle), and Case 3 (bottom).

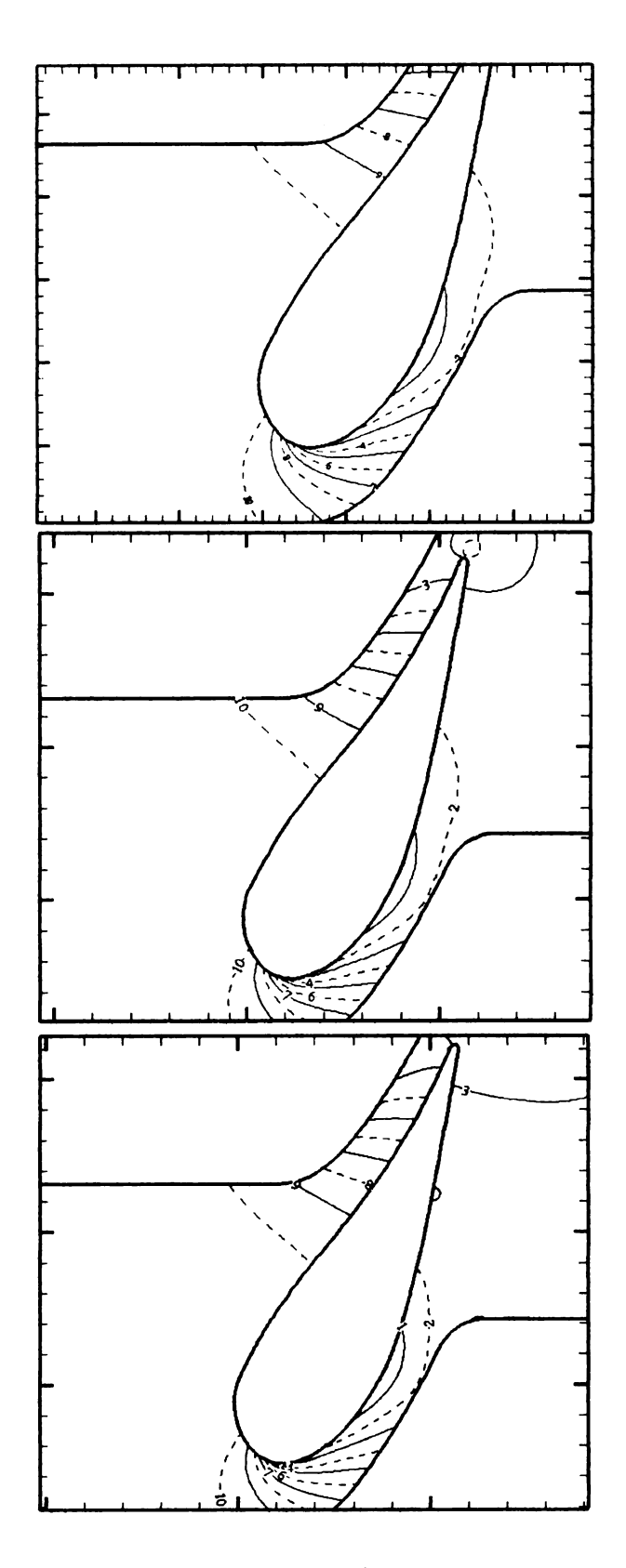


Figure 20: Contour plots of static pressure (gage) for Case 1 (top), Case 2 (middle), and Case 3 (bottom).

The plots of un-scaled residuals, wall effects in the boundary layer, and contour plots of the free stream all indicate that a converged solution has been attained and that a two-dimensional grid independent solution has been found through the majority of the vane passage. If computational expense was not an issue, the mesh from Case 3 would provide the best baseline for comparison of results throughout the vane passage. However, the results on the vane surface and through the passage in regions that are not affected by the separation zone (s/C < .7) are in very good agreement for all three cases. Thus, for the three-dimensional domain a compromise has been made on the mesh quality and the mesh documented in Case 1 will provide the most effective baseline for sweeping in the spanwise direction. This mesh, while not the highest quality for resolving the separation region when compared to Case 3, will provide adequate resolution of the boundary layer and core flow through the majority of the vane passage and will reduce computational resources for computing over the three-dimensional domain.

For comparison with the experimental results, Cases 4-8 are presented below.

Case 4 was solved with the realizable k-\varepsilon turbulence model and the residual plot is shown in Figure 21. Based on the convergence criteria set forth by FLUENT 5/6, it reached a converged solution. Based on the un-scaled plot shown below, all quantities have decreased by more than four orders of magnitude.

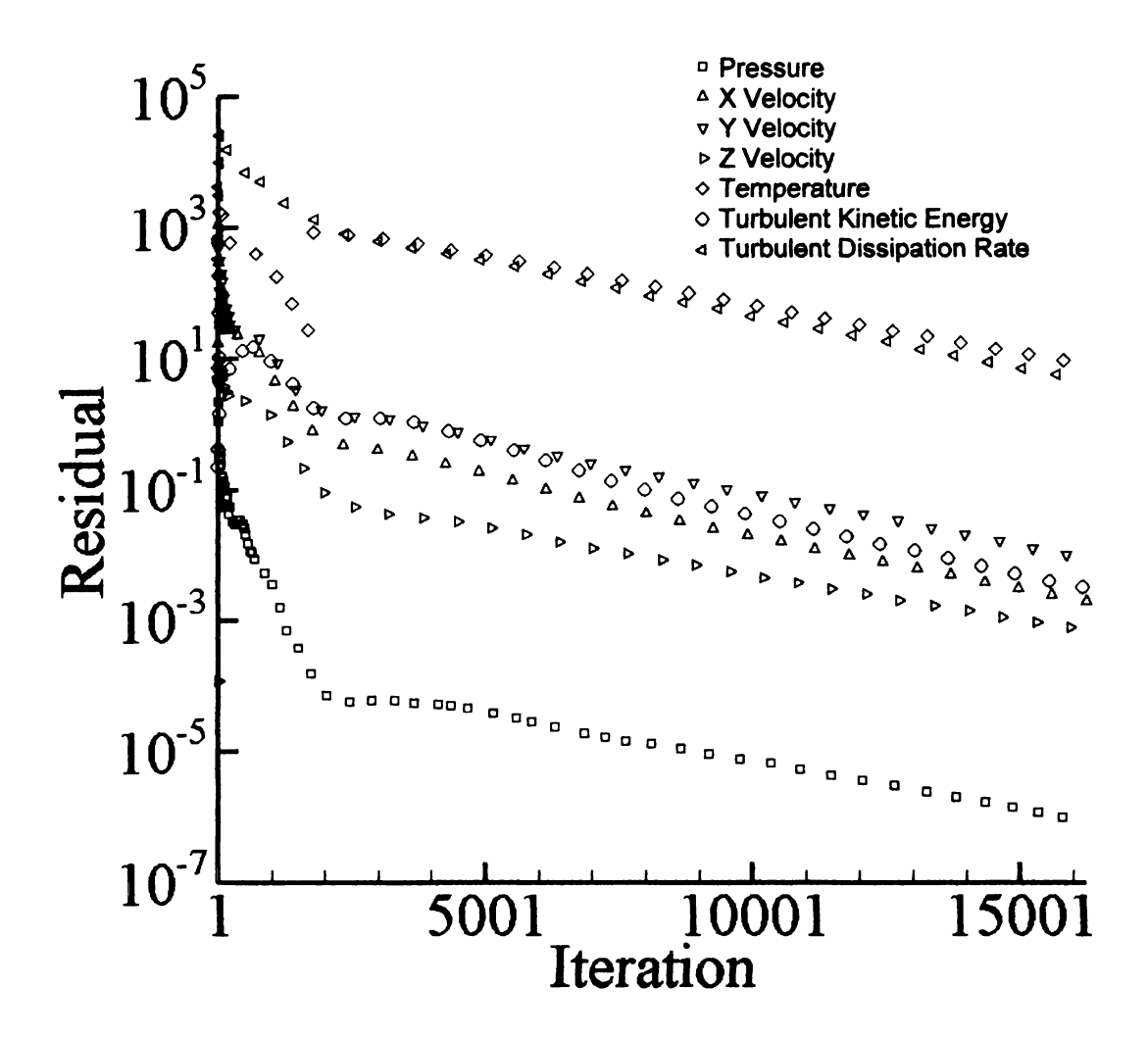


Figure 21: Residual plot for Case 4.

Case 5 was solved with the Reynolds stress model and its un-scaled residual plot is located in Figure 22. This case presented some issues with attaining a converged solution, which ultimately lead to requiring that it be initiated from the results of Case 4. Although convergence was not attained on the basis of scaled residual, Case 5 was able to reduce in magnitude by nearly two orders of magnitude.

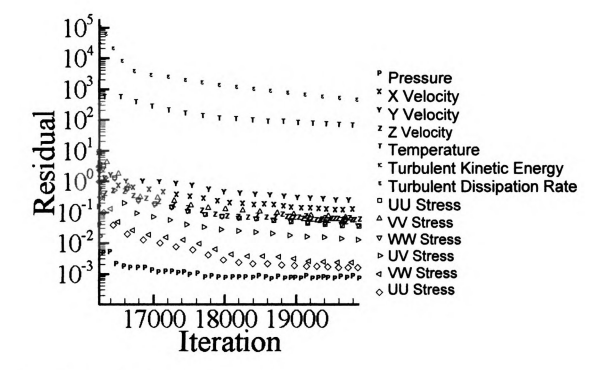


Figure 22: Residual plot for Case 5.

Case 6 was solved using the Spalart-Allmaras turbulence model. This case had no issues during the solution process and was able to attain a converged solution, based on the scaled residual criteria. The un-scaled residual plot is shown in Figure 23.

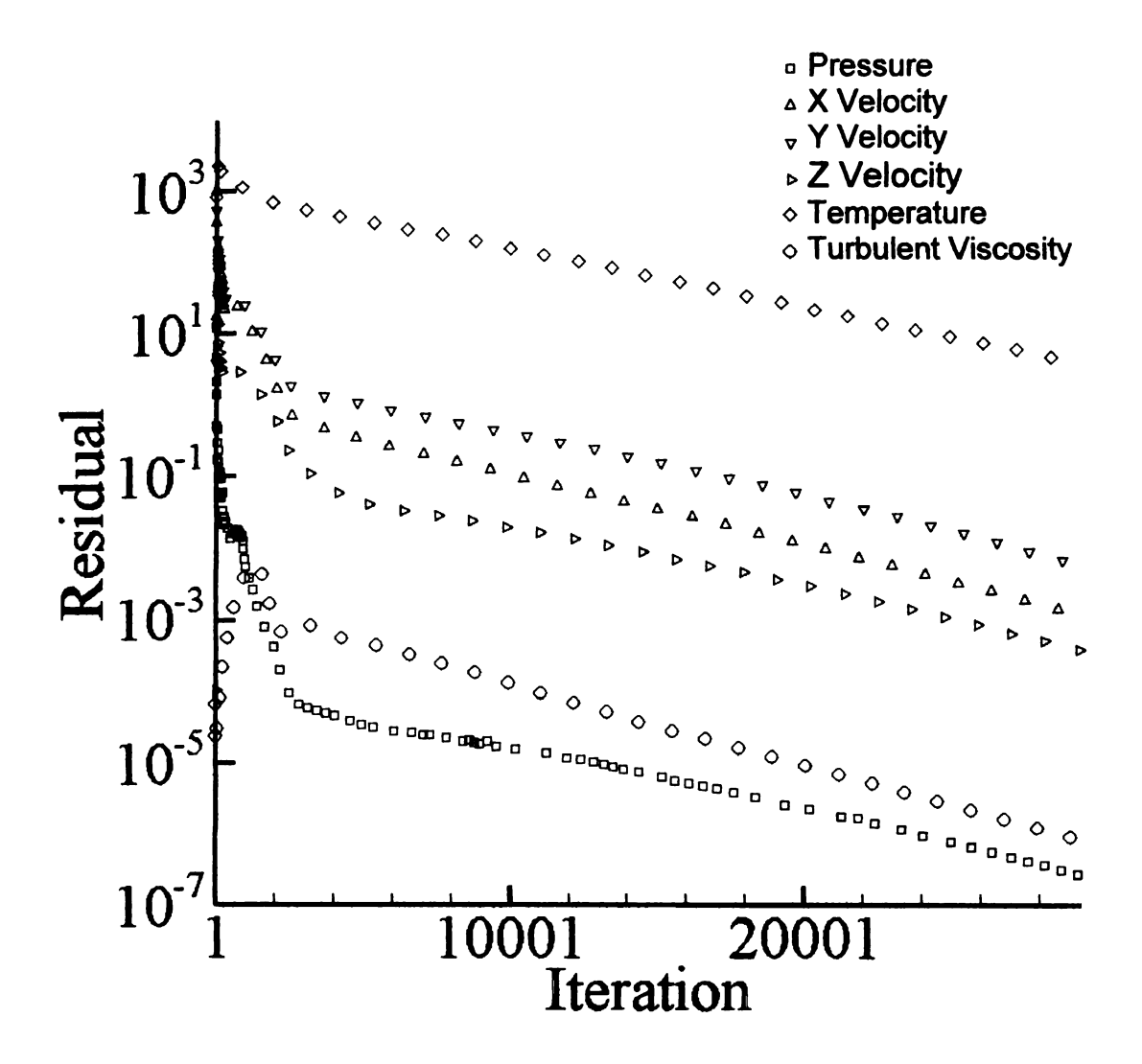


Figure 23: Residual plot for Case 6.

Case 7 was solved with the shear stress transport k-ω turbulence model. Minor adjustments were made to the under-relaxation parameters in order to attain a converged solution, with the un-scaled residual plot shown in Figure 24.

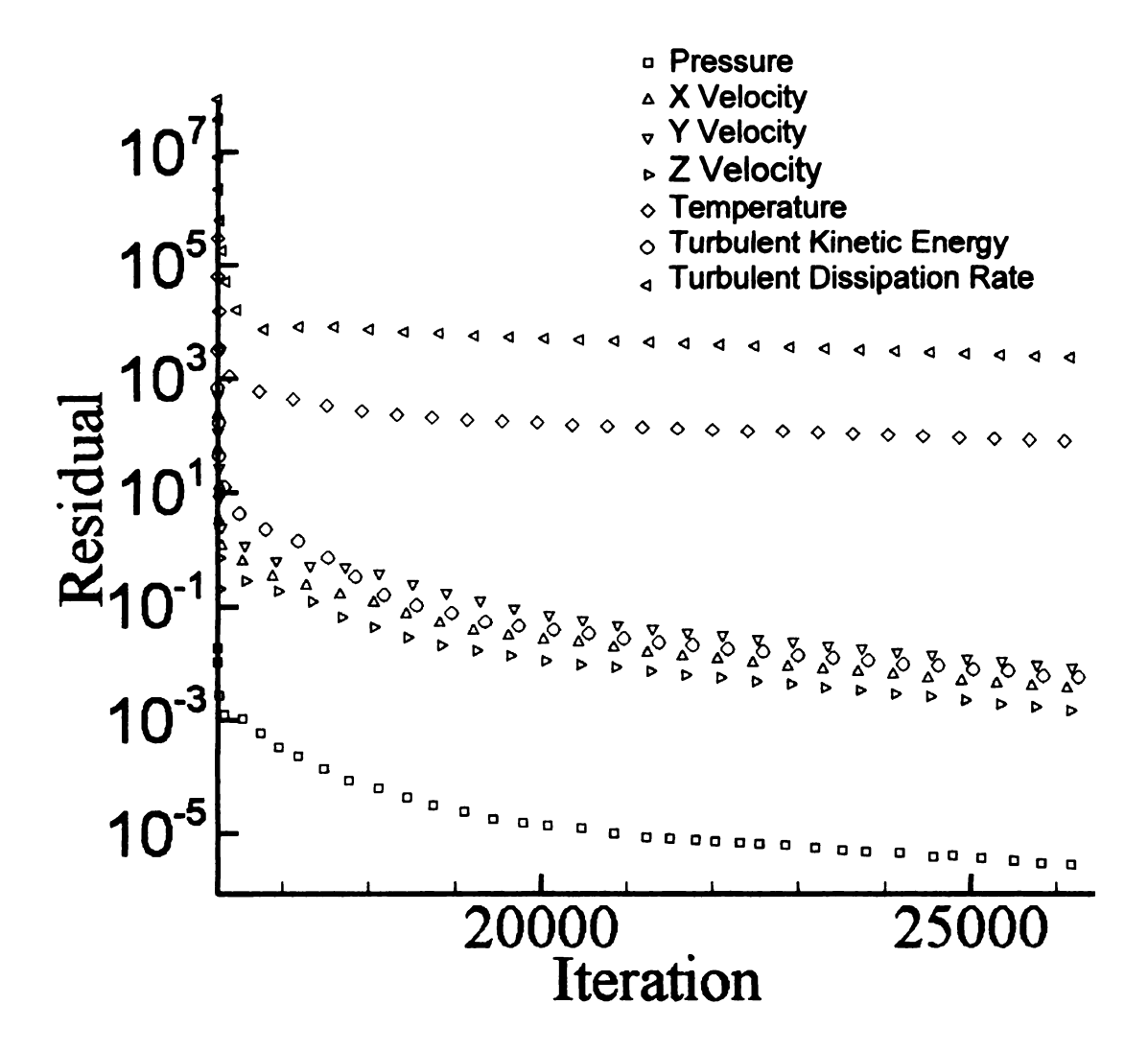


Figure 24: Residual plot for Case 7.

Case 8 was solved with Durbin's v^2 -f turbulence model. Due to convergence issues, this case was also initiated from the converged solution of Case 5. After initiating from Case 5, three adjustments were made to the under-relaxation parameters, as shown in Figure 25. Based on scaled residual criteria, a converged solution was not attained for Case 8. The un-scaled residual shown below did decrease by almost two orders of magnitude before reaching an asymptotic state in the solution process.

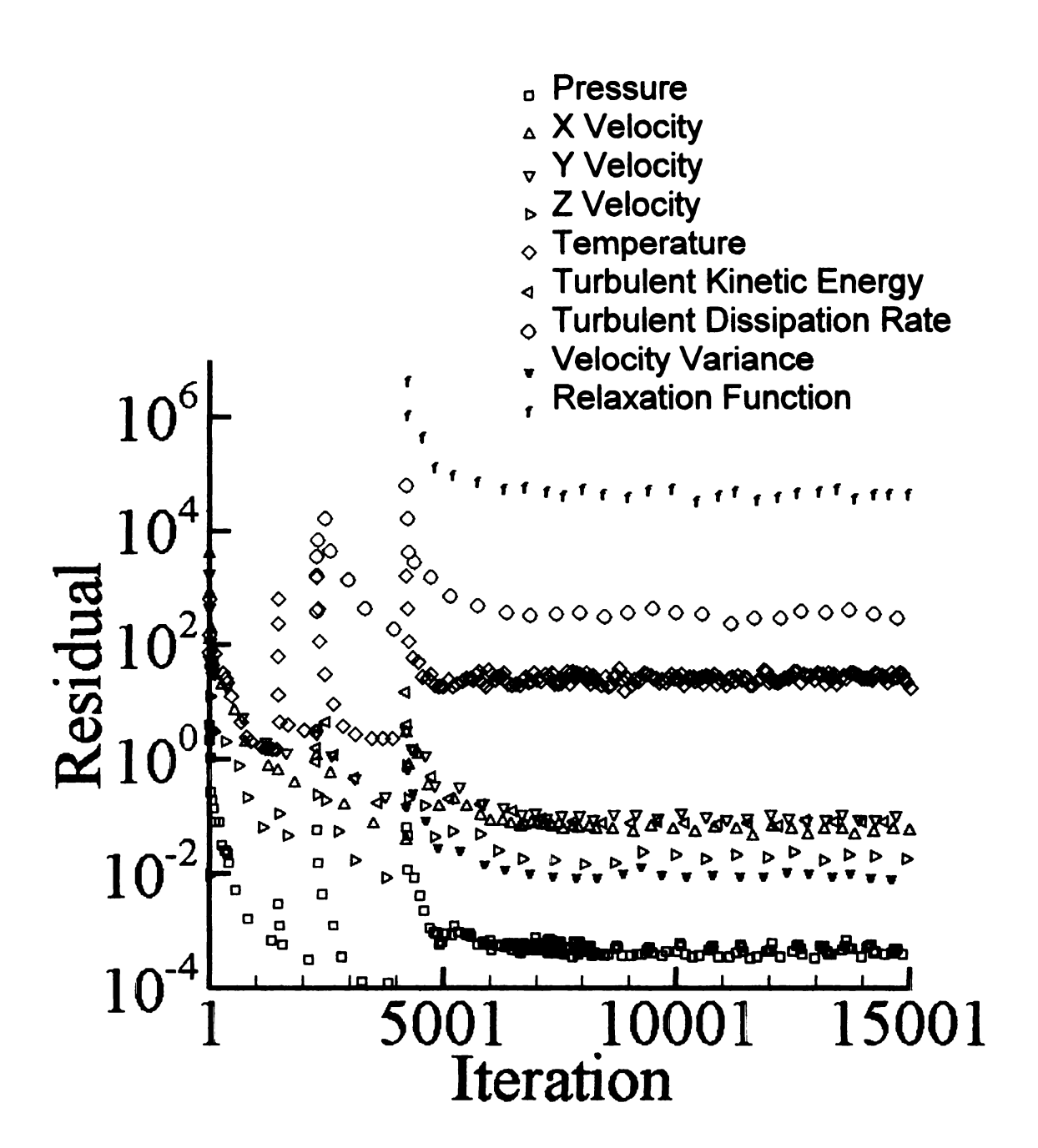


Figure 25: Residual plot for Case 8.

The following figures present the comparison of endwall heat transfer results between the experimental data and Cases 4-8, in units of W/m²-K. For these plots, the recorded endwall heat transfer results were measured with an infra-red camera, as described by Radomsky and Thole [3]. Due to the spatial averaging produced in the infra-

red camera measurements, the exact proximity of the recorded data to the endwall is not known. Thus, CFD results at multiple inner wall coordinates have been compared to the experimental measurements taken on the endwall of the vane by the infra-red camera.

The results for y+=1 are shown in Figure 26. Although the magnitudes are not in agreement, the trends appear to be following with the experimental data until the grid resolution is no longer adequate in resolving the separation region located in s/C > .75 on the suction side of the vane. Based on the difference between the peak magnitudes of experimental and CFD results, the spectral averaging does not agree well this close to the endwall.

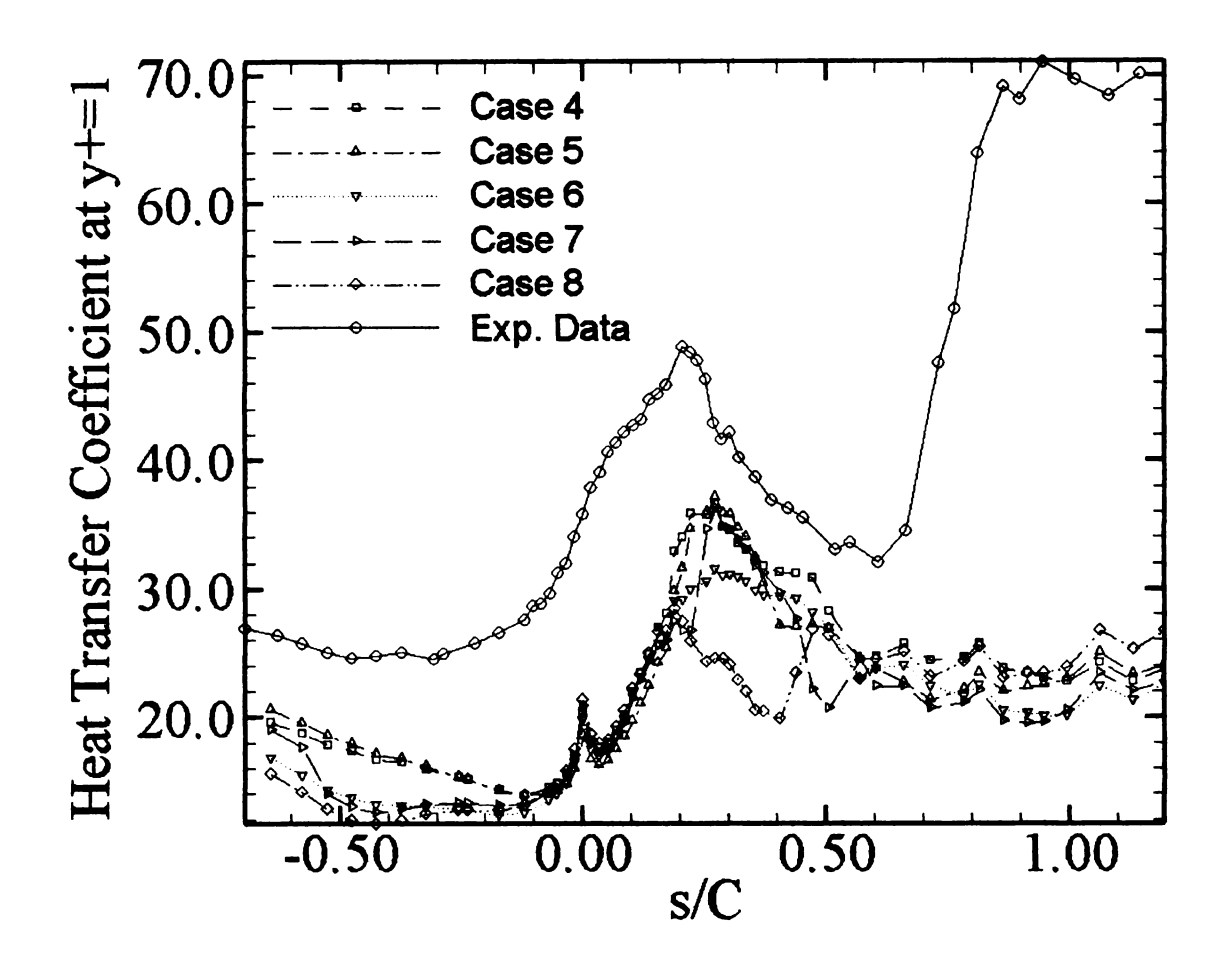


Figure 26: Endwall heat transfer results in local y-coordinates for y+=1 in the numerical domain.

The CFD data trends shown in Figure 27 are for y+=5. Here, all of the cases appear to show increasing heat transfer with increasing at s/C = -.3, but there is no real correlation that can be made between the cases and experimental data.

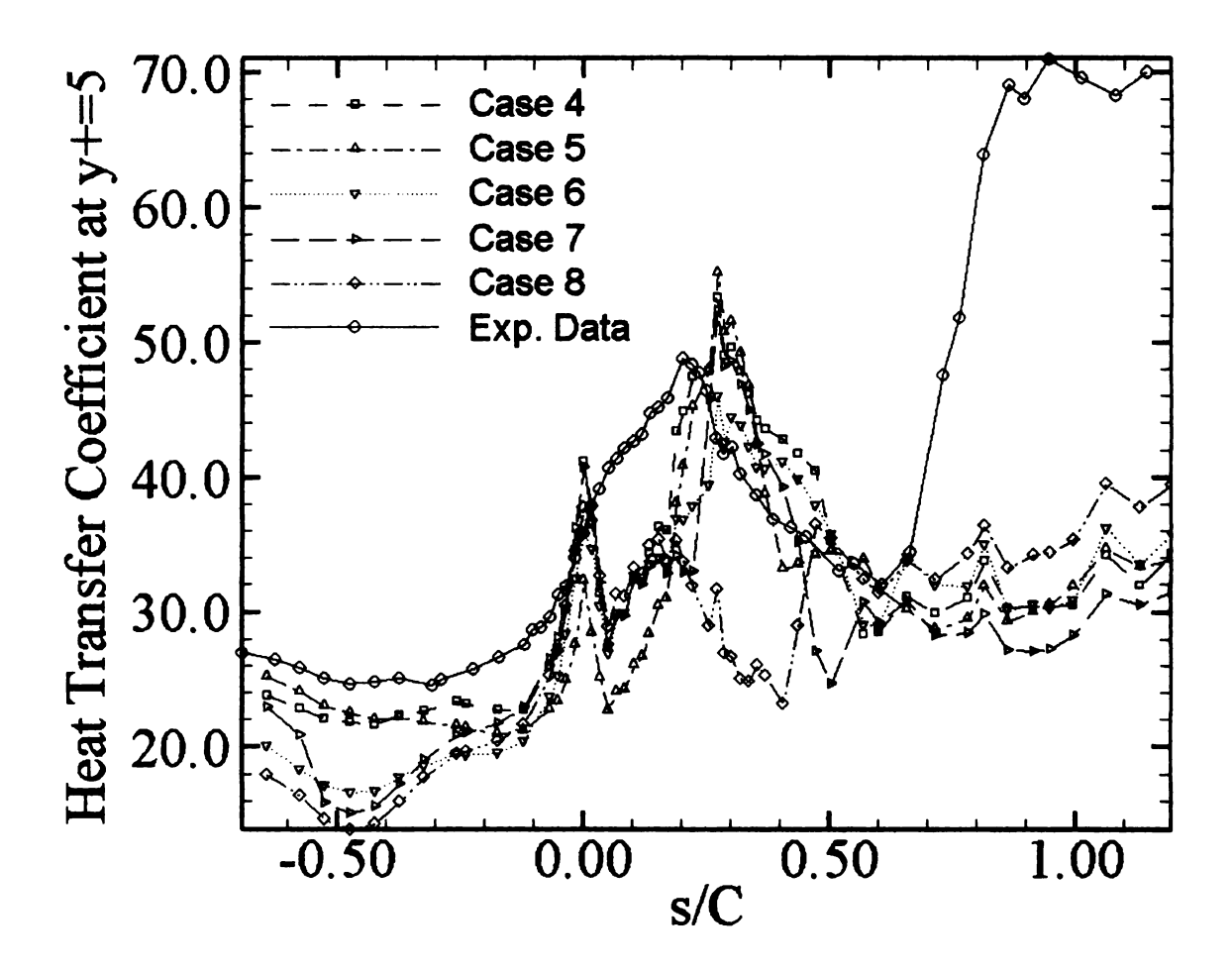


Figure 27: Endwall heat transfer results in local y-coordinates for y+=5 in the numerical domain.

Figure 28 has data at y+=10. At this location to the endwall, it appears that all cases expect for the Case 8 (v^2 -f model) are over predicting the heat transfer coefficient by more than 15% in the vicinity of s/C = .2 on the vanes suction side. Conversely, all cases show increasing heat transfer in the region of separation (s/C > .7). In this region, the more than 40% difference in heat transfer coefficient between experimental data and simulations can be attributed to lack of grid resolution.

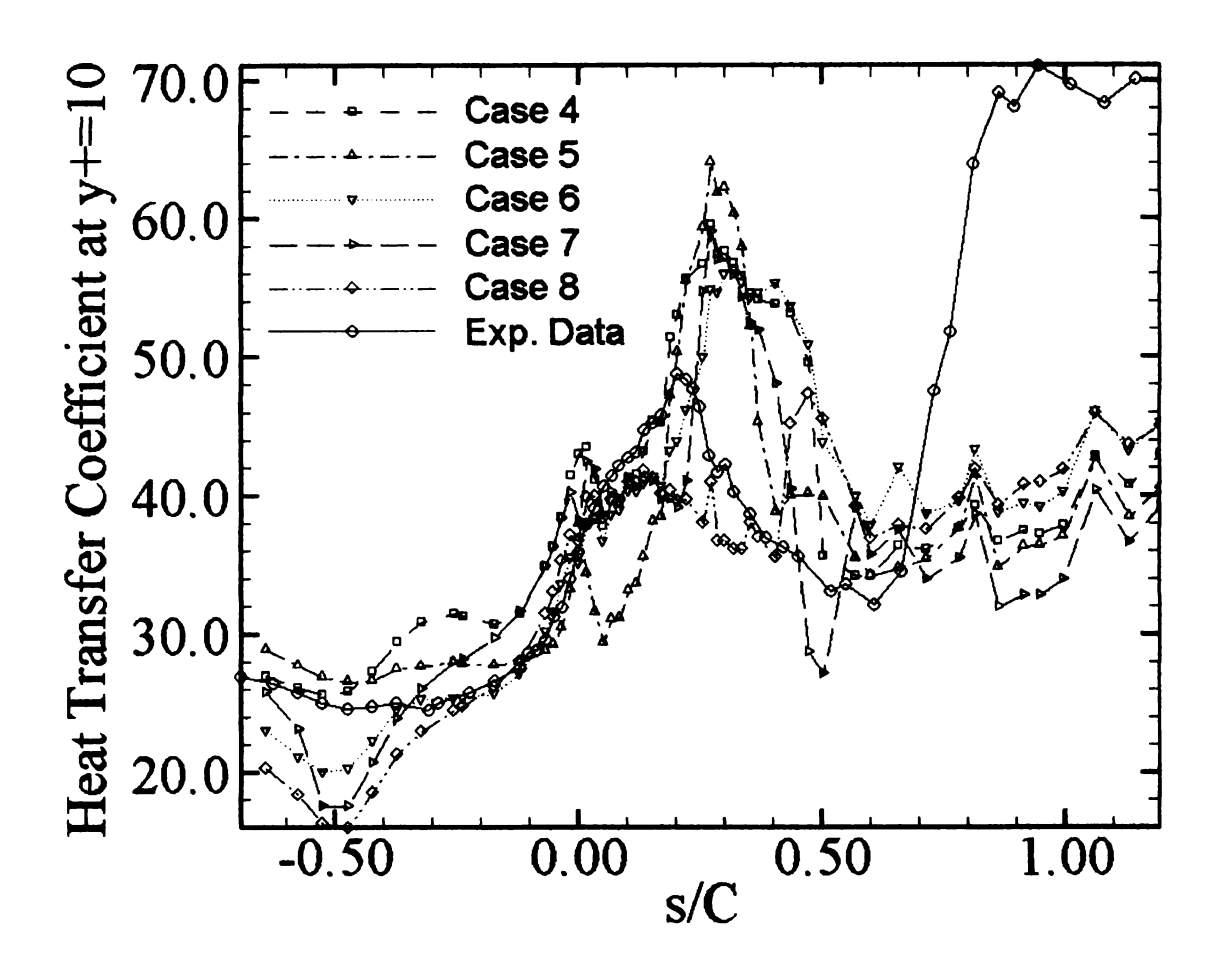


Figure 28: Endwall heat transfer results in local y-coordinates for y+=10 in the numerical domain.

Figure 29 shows the CFD data at y+=20. Again, all cases except for Case 8 are showing extreme over prediction of heat transfer in the vicinity of s/C = .2 on the vane. For Case 8, there is good correlation to the experimental data up to s/C = .1, at which the v^2 -f model starts to over predict the heat transfer coefficient by as much as 11%, with the peak value being shifted downstream by roughly .25 in non-dimensional vane length. Again, all cases predict increased heat transfer coefficient in the separated region as the data moves farther away from the endwall.

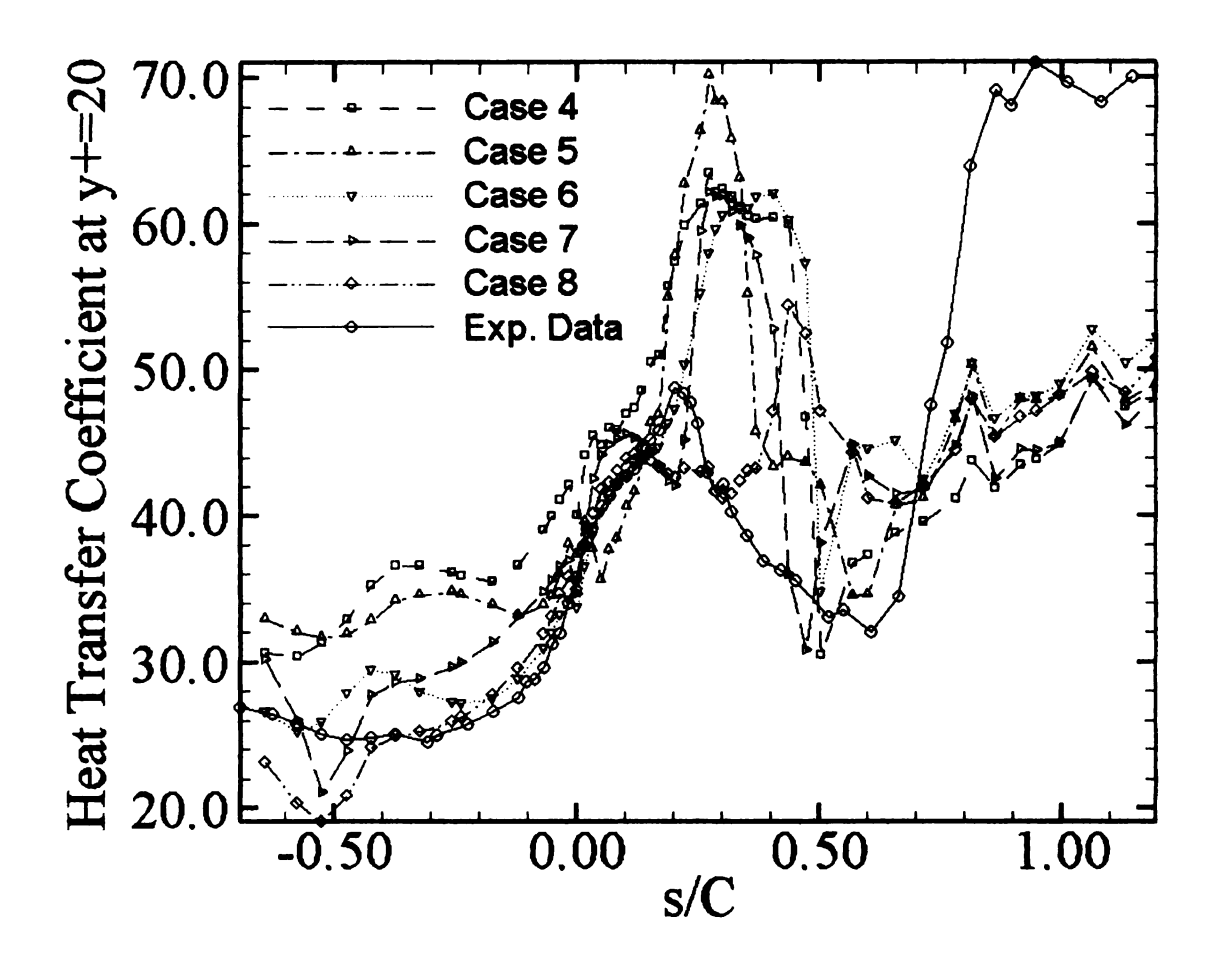


Figure 29: Endwall heat transfer results in local y-coordinates for y+=20 in the numerical domain.

Based on these results, the v^2 -f model appears to be the best turbulence model of those compared for predicting heat transfer through this vane passage. It is postulated that the spectral averaging of the infra-red camera measurement has in a sense smoothed out the experimental data, which is why the CFD predictions are so much more dramatic in change. However, when comparing the case that best fits the CFD results to the experimental measurements, the v^2 -f model is predicting within 11% peak difference through the majority of the vane passage. Had the grid resolution been better in the region of separation, this may have been seen throughout the entire passage.

In comparing the turbulent models to each other, it is obvious that the v^2 -f model was best equipped for predicting the heat transfer in the endwall region of this passage. However, if turnaround time is more important than accuracy, it may be more effective to use a turbulence model with fewer transport equations to establish a rough idea of what the aerodynamics and heat transfer look like in the given geometry. Table 4 lists all of the cases ran and breaks down the solution times.

Case Number	Domain	Turbulence Model	Number of Elements	Iterations to Converged Solution	Time per Iteration (seconds)	Time to Converged Solution (days)
1	2D	Spalart-Allmaras	50,396	27,657	1	0.3
2	2D	Realizable k-ε	22,060	25,955	1	0.3
3	2D	Realizable k-ε	200,544	40,520	5	2.3
4	3D	Realizable k-ε	1,511,880	16,243	55	10.3
5	3D	Reynold's Stress Model	1,511,880	19,892	195	44.9
6	3D	Spalart-Allmaras	1,511,880	29,442	25	8.5
7	3D	Shear Stress Transport k-ω	1,511,880	26,527	60	18.4
8	3D	Durbin's V2-f	1,511,880	11,060	150	19.2

Table 4: Computational information for Cases 1-8.

Even though the Spalart-Allmaras model requires half of the time per iteration when compared to the realizable k- ϵ model, it took nearly twice as many iterations to converge. That being said, the realizable k- ϵ model was probably the most stable of the turbulence models used in this study. In the three-dimensional domain, it required the fewest number of iterations to reach a converged solution based on scaled residual criteria and required minimal, if any, adjustments to the under-relaxation factors. The Reynolds stress model and the v^2 -f model were both very unstable during the early

iterations and required initialization from a converged solution in order to reach convergence.

In closing, this project has been very fulfilling. The grid independence study provided critical learning skills required for quality mesh generation. Performing the simulations over the same numerical domain with five different turbulence models has supplied a broad sense of the physics at work in this vane passage as well as expanded my knowledge base in the field of turbulence.

REFERENCES

- [1] Radomsky, R.W., and Thole, K.A., 2000, "Measurements and Predictions of a Highly Turbulent Flowfield in a Turbine Vane Passage," ASME Journal of Fluids Engineering, 122, pp. 666-676.
- [2] Radomsky, R.W., and Thole, K.A., 2000, "Effects of High Freestream Turbulence Effects on Endwall Heat Transfer for a Gas Turbine Stator Vane," ASME Journal of Turbomachinery, 122, pp. 255-262
- [3] Radomsky, R.W., and Thole, K.A., 2000, "High Freestream Turbulence Effects on Endwall Heat Transfer for a Gas Turbine Stator Vane," ASME Paper No. 2000-GT-0201, Turboexpo Meeting, May 2000.
- [4] Radomsky, R.W., and Thole, K.A., 1998, "Detailed Boundary Layer Measurements on a Turbine Stator Vane at Elevated Freestream Turbulence Levels," ASME Paper No. 2001-GT-0169
- [5] FLUEN User's Guide, 1998, Release 5.0, Fluent Inc., Lebanon, N.H.
- [6] Kang, M.B., Kohli, A., Thole, K.A., 1999, "Heat Transfer and Flowfield Measurements in the Leading Edge Region of a Stator Vane Endwall," ASME Journal of Turbomachinery, 122, pp. 558-566.
- [7] Gu, X., Schock, H.J., Shih, T.I-P., Hernandez, E.C., Chu, D., Keller, P.S., and Sun, R.L., 2001, "Grid-Quality Measures for Structured and Unstructured Meshes," AIAA Paper 2001-0652, Aerospace Sciences Meeting, Jan. 2001.
- [8] Qin, Y., Shih, T.I-P., 2002, "A Discrete Transport Equation for Error Estimation," AIAA Paper 2002-0906, Aerospace Sciences Meeting, Jan. 2002.
- [9] Van Driest, E.R., "On Turbulent Flow Near a Wall," Journal of Aeronautical Science, Vol. 23, No. 11, 1956, pp. 1007-1011 and 1036.

- [10] Pope, S.B., 2000, "Turbulent Flows," Cambridge University Press.
- [11] Shih, T.I-P., 1994, "Fundamentals of Computational Fluid Dynamics," Michigan State University, Department of Mechanical Engineering.

3 1293 02956 4337